Spring 5-31-1995

Integration of pneumatic fracturing and in situ vitrification in coarse grained soils

Sean Thomas McGonigal
New Jersey Institute of Technology

Recommended Citation

ABSTRACT

INTEGRATION OF PNEUMATIC FRACTURING
AND
IN SITU VITRIFICATION IN COARSE GRAINED SOILS

by
Sean Thomas McGonigal

This thesis investigates conceptual integration of the Pneumatic Fracturing (PF) process with In Situ Vitrification (ISV) for remediation of contaminated soil. Integration will permit ISV melts to be initiated below the ground surface and extend the depth of the ISV process.

Bench scale experiments were conducted in 4.9 ft^3 (0.14 m^3) Plexiglas tanks filled with a test soil that was specifically blended to simulate the Hanford Formation in Richland, WA. Discrete pneumatic fractures were successfully created and filled with the ISV starter path material. Conductivity measurements made across two graphite electrodes exhibited a pre-fracture soil resistance of 427 ohms, which was reduced to an average of 0.80 ohms after fracture injection.

A model was developed to predict transport distance of the ISV starter path media in pneumatically induced fractures. The model estimates fracture propagation distance using a finite-difference approach, as well as the critical fluid velocity necessary to keep the starter path media suspended. Model calculations show the effective radius of the integrated process should range up to several meters in the Hanford Formation. The thesis concludes with operational recommendations for full scale application.

INTEGRATION OF PNEUMATIC FRACTURING
AND
IN SITU VITRIFICATION IN COARSE GRAINED SOILS

by
Sean Thomas McGonigal

A Thesis
Submitted to the Faculty of
New Jersey Institute of Technology
in Partial Fulfillment of the Requirements for the Degree of
Master of Science in Environmental Engineering

Department of Civil and Environmental Engineering

May 1995

APPROVAL PAGE

INTEGRATION OF PNEUMATIC FRACTURING
AND
IN SITU VITRIFICATION IN COARSE GRAINED SOILS

Sean Thomas McGonigal

Dr. John R. Schuring, Thesis Advisor   Date
Professor of Civil and Environmental Engineering, NJIT

Dr. Paul C. Chan, Committee Member   Date
Professor of Civil and Environmental Engineering, NJIT

Dr. Victor Ososkov, Committee Member   Date
Research Chemist, Center for Environmental Engineering and Science, NJIT

BIOGRAPHICAL SKETCH

Author: Sean Thomas McGonigal

Degree: Master of Science in Environmental Engineering

Date: May 1995

Undergraduate and Graduate Education:

- Master of Science in Environmental Engineering
  New Jersey Institute of Technology, Newark, NJ, 1995

- Bachelor of Science in Civil Engineering
  Syracuse University, Syracuse, NY, 1991

Major: Environmental Engineering

This thesis is dedicated to my parents,
John A. McGonigal and Anne T. McGonigal
and to the memory of my
grandfather John J. McGonigal
and good friend Matthew S. Shrodo

ACKNOWLEDGMENT

TABLE OF CONTENTS

TABLE OF CONTENTS
(Continued)

LIST OF TABLES

LIST OF FIGURES

CHAPTER 1

INTRODUCTION

1.1 General Information

One of the most critical issues in the world today is the condition of the environment. The environment has a profound effect on human health and on other aspects of the quality of life. An important element of the environmental condition is how to manage, treat, and dispose of hazardous wastes. This is becoming increasingly important, as advances in technology create more complex wastes that present greater hazards to human health and the environment.

Today, a concerted effort is being made to remediate contaminated sites. Most of these sites have contamination due to past disposal practices that were either irresponsible or were once considered "state of the art", but are now known to be inadequate. There are numerous contaminated sites in the United States, over 1,296 sites of which are on the National Priority List (NPL), and 54 more are proposed to be added as of February, 1995 (Personal communication, 1995). In New Jersey alone, there are 6,000 known contaminated sites (NJDEP) of which 107 of these sites are presently on the NPL. The NPL sites pose the greatest threat to human health and the environment, and fall under the Comprehensive Environmental Response, Compensation, and Liability Act (CERCLA) of 1980, better known as the Superfund program. Despite the attention of CERCLA, relatively few sites have actually been remediated due to the limited number of technologies available and the complexity of the hazardous waste sites.

To bolster the number of remedial technologies, as well as to address the other problems with the Superfund program, the Superfund Amendments and Reauthorization Act (SARA) were passed in 1986. Out of SARA, the Superfund Innovative Technology Evaluation (SITE) program was created to enhance the development and demonstration of innovative technologies for remediation of Superfund sites. The SITE program has mostly focused on in situ remedies because of their inherent cost effectiveness. Primary technologies in this program have included soil vapor extraction, air sparging, hot gas injection and in situ bioremediation. These innovative technologies, as well as more established technologies such as pump and treat, are not panaceas. A number of contaminant and site characteristics may reduce the effectiveness of these remedial technologies, or even preclude their use. For example, contaminated sites containing geologic formations with low hydraulic conductivity are inherently difficult to treat with in situ techniques. Such sites require some type of enhancing process if the primary in situ technologies are to be effective.

One new enhancing technique developed over the last several years is pneumatic fracturing (PF). As an enhancement technology, it is necessary to combine PF with one or more remediation technologies to effect a cleanup. To date, PF has been successfully coupled with conventional pump and treat, soil vapor extraction and in situ bioremediation. The increased fluid flow resulting from the artificially created fractures is the primary enhancing mechanism of pneumatic fracturing.

1.2 Objective and Scope

It is the objective of this study to integrate PF with in situ vitrification (ISV), which is a molten glass process developed at Department of Energy's (DOE) Pacific Northwest Laboratories (PNL) in the early 1980's. The integration of PF with ISV is not typical of past applications of pneumatic fracturing for two reasons. First, the site to be "fractured" contains predominantly coarse grained soils (Hanford Formation), which do not require permeability enhancement. Traditionally PF has been applied to formations with low hydraulic conductivities, such as clayey soils and rock formations, to increase permeability. Second, the principal purpose of the pneumatic fracturing system in this project is to inject a dry, "starter" media into the fracture. Presently, the ISV process places the starter media on the ground surface to initiate its process, but to date the process has been effective to a depth of about 5 meters. By utilizing PF to inject the dry media at deeper levels, it can extend the effective depth of the ISV process. It should be noted that this is the first attempt at using the pneumatic fracturing process to inject a dry media into a coarse grained formation.

The objectives and scope of this study are therefore to:

1)   Review the separate PF and ISV technologies, and develop an approach to integrate them in the coarse grained Hanford Formation.

2)   Perform bench scale laboratory studies to simulate the integrated process in a surrogate soil blended to resemble the Hanford Formation.

3)   Define the critical soil parameters that may affect the ability to fracture and inject media.

4) Investigate the mechanisms of dry media transport in air, and adapt a transport model to the integrated PF/ISV process.

5) Develop recommendations for application to a full scale pilot demonstration of the integrated PF/ISV process at the Hanford site.

CHAPTER 2

REVIEW OF TECHNOLOGIES TO BE INTEGRATED

2.1 Pneumatic Fracturing

2.1.1 Technology History

Development of pneumatic fracturing began in the Spring of 1988 at the Hazardous

Substance Management Research Center (HSMRC) at the New Jersey Institute of

Technology (NJIT) with the objective of enhancing remediation of contaminated sites

with low permeabilities. Bench scale studies initially investigated the effect of

pneumatic fracturing on soil vapor extraction. Plexiglas vats were packed with

contaminated soil at a known concentration, and vapor extraction was applied both with

PF, and without PF. The results consistently showed that PF increased the rate of

removal by 170% to 360% as compared with the results of vapor extraction alone

(Papanicolau, 1989; Shah, 1991).

Field pilot demonstrations of PF began in 1989, and since then 12 sites in various

geologic formations have been successfully fractured and have achieved increased

permeability. These sites include both clean and contaminated sites, two of which were

U.S.EPA SITE demonstrations. One of the SITE demonstrations, conducted at a

petroleum refinery in Pennsylvania, investigated the integration of pneumatic fracturing

and in situ bioremediation (U.S. EPA, 1995). In this project, pneumatic fracturing was

used to increase the permeability of the formation as well as deliver nutrients to the

microorganisms. The other SITE demonstration, performed in Hillsborough, NJ, focused

on the ability of pneumatic fracturing to enhance soil vapor extraction in removing chlorinated organics (U.S. EPA, 1993).

Pneumatic Fracturing was patented in July, 1991 (U.S. Patent # 5,032,042), and is now commercially available through Accutech Remedial Systems (ARS) of Keyport, NJ. Accutech has incorporated PF into an integrated remediation system known as Pneumatic Fracturing Extraction (PFE). ARS has a non-exclusive license to apply PF, and discussions are underway with other potential licensees.

Future areas of research include integration of PF with air sparging and in situ chemical reduction, as well as other treatment technologies.

2.1.2 Methodology

Pneumatic Fracturing is the process of injecting a high pressure gas, usually air, into a contaminated geologic formation at a pressure which exceeds its natural in situ stresses, and at a flow rate that exceeds the permeability of the formation. This causes failure of the medium and creates a fracture network that radiates from the injection point. Once established, the fractures increase the permeability of the formation, thereby enhancing the flow of fluids for more efficient contaminant removal (Schuring and Chan, 1993). Figure 2.1 displays the permeability enhancement of fine grained soil and sedimentary rock formations (HSMRC et al., 1994).

Prior to fracturing, a thorough site characterization is vital since the geologic formation and its properties are critical to the success of fracturing. Exploratory boreholes should be drilled and a detailed analysis made of the recovered samples. The

(a) Fine-grained Soil Formations

(b) Sedimentary Rock Formations
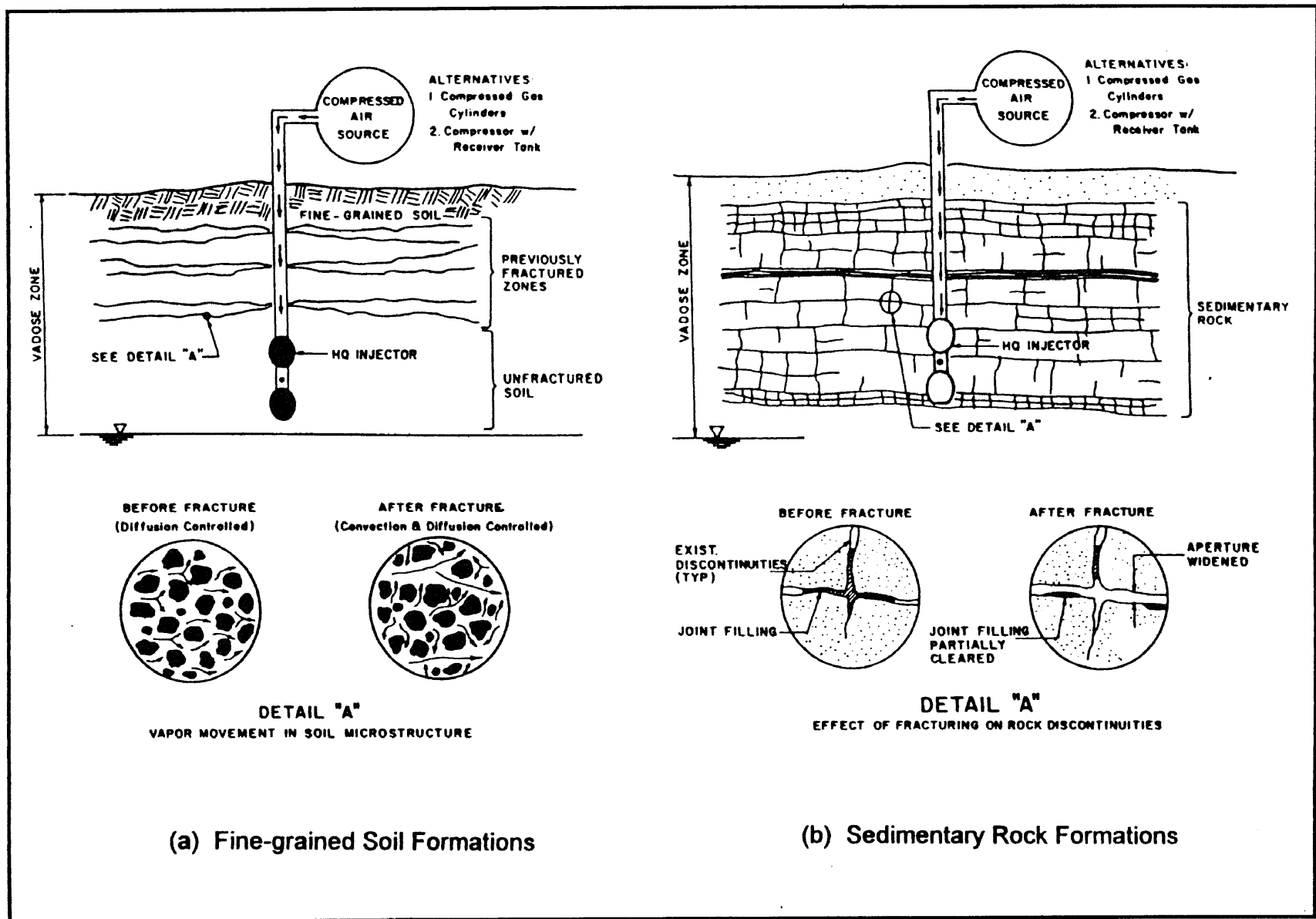
Figure 2.1 Pneumatic Fracturing Concept

depth to water table should be accurately determined and in situ permeability testing should be performed if possible. In soil formations, laboratory analyses should be performed including grain size analysis, natural moisture content, Atterberg limits and strength testing. Contaminant identification, concentration and distribution are also essential data for contaminated sites.

After gathering the data from the exploratory boreholes, injection and extraction wells are strategically installed according to site hydrogeology and contaminant distribution. A high flow (HQ) injector is then placed into the injection well, which is a device that directs pressurized air radially into the formation. To insure that the HQ injector remains stationary in the well and that the air is concentrated at the desired level, inflatable packers are positioned above and below the nozzle, which isolate a two foot interval in the well for each injection.

The HQ injector is then connected to the air source by a high pressure hose. The compressed air source is a battery of air cylinders connected together by a manifold system, which allows them to work simultaneously. The pressure and flow of the air is controlled by regulators and valves. The actual fracture injection is relatively brief and is typically less than 30 seconds.

Since pneumatic fracturing is a relatively new technology, monitoring devices are imperative to increase understanding of the mechanisms involved in the process. They also help visualize the reaction of the formation, which is difficult to observe directly. The monitoring devices include a flow manifold, pressure-flow indicators, tiltmeters and a borehole video camera. The flow manifold is a series of flow meters used in

conjunction with a vacuum unit to determine pre- and post-fracture air permeability of the formation. Pressure-flow indicators include pressure gauges and rotameters which establish if a connection was made with an outlying well. The tiltmeters measure ground surface heave and allow the data to be downloaded into a computer. Typically, twelve tiltmeters are used during each injection and provide the data to produce a contour map of surface heave. The borehole video camera allows the observation of the borehole before and after fracturing in order to directly observe the effects of the injections, as well as helping to establish a fracture strategy.

As expected, pneumatic fracturing has varying effects on different formations. Fine grained soils, which usually have low permeability, develop channels which increase the permeability and expose additional surface area in the formation. Sedimentary rocks develop wider fractures as a result of the PF process, thereby improving connectivity of the existing network of discontinuities. In the past, application of PF to coarse grained soils has been limited to rapid aeration of the formation.

2.2 In Situ Vitrification

2.2.1 Technology History

In situ vitrification was patented in the United States (U.S. Patent # 4,376,598) in 1983 and is also patented in Canada, Great Britain and France. Battelle Memorial Institute obtained the worldwide license rights for all non-radioactive applications and created a new company in 1988, Geosafe Corporation, to commercialize the process.

Initially, the ISV process was developed to treat soil contaminated with radioactive materials, but it is also applicable to organic and heavy metal contaminants. Presently, the process is used to treat contaminated soil, process sludges and tailings piles, and it is being evaluated for treatment of uncontrolled hazardous waste sites containing drums and buried tanks that contain a hazardous heel in the form of either sludge or slat cake (Dragun, 1991). ISV is also being tested as a method to create horizontal and vertical subsurface barriers and is being considered for civil engineering applications such as soil solidification.

The first full scale test on radioactive wastes were done at a landfill-like site. The test was conducted in 1990 by U.S. DOE's Idaho National Engineering Laboratory. (INEL) at their facility in Idaho Falls, ID in cooperation with PNL. Laboratory scale and pilot scale tests were performed at PNL's Hanford site in Richland, WA. These tests were also the first to evaluate ISV on buried high-metal content wastes.

Presently, ISV is able to treat wastes to a depth of 5 to 6 meters, which is acceptable for most commercial sites and some DOE sites. Researchers are now investigating methods to extend the ISV process to a depth of 10 meters, which would facilitate more DOE applications. The waste materials that have successfully been treated include 13 metals, 9 radioactive elements, 10 liquid organic and 11 solid organic compounds (Dragun, 1991).

2.2.2 Methodology

In situ vitrification is a thermal treatment process that converts contaminated soil into a chemically inert and stable glass and crystalline product. The process is based on the principle of joule heating, which is electrical current transformed into heat. The process continues to increase as the current passes through the molten mass. The electricity is passed to the formation by four graphite electrodes, that contain a molybdenum core, arranged in a square pattern. The electrodes are installed into the ground and slowly fed into the subsurface until the desired depth of the melt is attained. The formation should be as dry as possible to minimize power. Since most soils are not conductive when devoid of water, a starter path of a glass frit and graphite mixture is placed between the electrodes on the ground surface. The starter path is a one to one ratio of glass frit to graphite. The graphite provides the conductivity between the electrodes, and the glass frit provides the silica necessary to initiate the glassification or vitrification of the soil.

An electric potential is then applied to the electrodes and the resulting power heats the starter path and the surrounding soil to 2000°C. This is well above the temperature to initiate soil melting, which is 1100°C to 1400°C. The starter path is consumed by oxidation and the current flows through the conductive molten soil. The melt grows at rate of about 1 to 2 inches per hour to depths of 5 to 6 meters and outwards to about 50% of the electrode spacing (Dragun, 1991).

As the melt grows, non-volatile, semi-volatile elements and radionuclides that are present become indefinitely immobilized. The high temperature of the process destroys organics by pyrolysis. The by-products of pyrolysis migrate to the surface of the melt

where they combust in the presence of oxygen. The hood that covers the melt area is operated under a slight vacuum which pulls the gases through a treatment system. The complexity of the treatment system depends entirely on the gaseous constituents encountered. The solidified melt can remain in the ground as it has passed the most stringent U.S. EPA leachability tests. The site is then backfilled because of the subsidence during the vitrification process. Volume reduction ranges between 20% to over 40% depending on the type of waste (Timmons et al., 1990).

2.3 Proposed Concept of Integration

To effectively apply ISV to a broader range of sites, the melt needs to be extended deeper than the existing limit of 5 to 6 meters, since many sites have contamination below this depth. Therefore, several options have been considered to facilitate this extended application, one of which is the PF technology. It is believed that the PF process can introduce a lens of the graphite and glass frit starter path into the subsurface to continue the melt deeper, possibly to 10 meters, which is the depth necessary to remediate most DOE sites. It may also enable the process to "surgically" melt specific areas of a formation. For example, if contamination is between 8 and 15 meters deep in the subsurface, melting the soil above that depth would be an inefficient method of treating the soil in the contaminated zone. Therefore, if PF can deliver a conductive lens in the contaminated range, the melt would encompass only the soil that needs treatment.

Although the PF process has never been used to inject a dry media into a fracture in a field application, it has been successfully achieved at a bench scale level. These

include the injection of pelletized nutrients and silica sand into fine grained soil. The site proposed for the integration of PF and ISV, however, is a coarse grained formation. To date, the only function that PF has served in this type of formation is rapid aeration.

Therefore, a bench scale study was initiated to determine if a conductive starter path could be introduced into the formation. The two methods chosen for investigation were: 1) fracturing the formation and subsequently filling it with the graphite and glass frit; and 2) injecting the starter path through the interstices of an unfractured formation.

The first method of starter path distribution is a unique application, as fracturing a coarse grained formation has never been attempted. The high permeability of the formation will allow excessive leakoff of injected air into the formation, thus reducing pressure and limiting the radius of fracture. However, if a fracture is created, it is believed that the graphite will easily fill the void since it is self-lubricating and should transport efficiently. The conductivity of the injected lens is also a critical parameter to be studied, as it is not sufficient just to fill the fracture with the graphite/glass frit mixture. Significant contact must be made between all of the electrodes and the graphite portion of the mixture to initiate the melt.

Injecting a starter path into the interstices of the formation is another mode of creating the conductive lens, although less promising. The ability of PF to force the injected media a significant distance through the pores of the formation is not anticipated in zones of finer grained materials. However, if a coarse zone is encountered, interstitial transport may be a viable option.

CHAPTER 3

APPROACH OF LABORATORY STUDY

This chapter will discuss the test approach to the laboratory studies. The laboratory studies were a significant part of determining the effectiveness of the PF/ISV integration process. These studies provided both quantitative and qualitative verification of whether the integrated process could successfully establish a conductive path between electrodes at the bench scale.

The chapter begins with Section 3.1, which describes the design and preparation of the surrogate test soil used to conduct the laboratory tests. Section 3.2 outlines the experimental set up and procedure of the tank tests. These tests were used to explore the feasibility of fracturing the highly permeable surrogate test soil, as well as injecting sand into the fractures. Section 3.3 details the experimental set up and procedure of the conductivity tests which entailed measuring conductivity across two electrodes following the injection of the graphite/glass frit media. Section 3.4 discusses the horizontal infiltrometer test set up and procedure used to study the ability of the graphite/glass frit mixture to travel through the interstices of the surrogate test soil. The segregation test set up and procedure, detailed in Section 3.5, investigates the degree of separation between the graphite and the glass frit during injection.

3.1 Design and Preparation of Surrogate Test Soil

3.1.1 Analysis of Hanford Soil

A series of laboratory tests were performed on samples of the Hanford Formation soil to determine its physical properties. These tests included grain size analysis, Unified Soil Classification System (USCS) classification, Atterberg limits, organic content, specific gravity, and standard Proctor density. All testing was performed following the standard methods of the American Society for Testing and Materials (ASTM). Results of these tests are summarized in Table 3.1. The grain size distribution of the Hanford soil is shown in Figure 3.1.

3.1.2 Preparation of Surrogate Test Soil

Since it was not feasible to ship the required amount of Hanford Formation soil needed for the bench scale tests, 2000 lb (907 kg) of surrogate test soil was prepared to simulate the site soil. The grain size distribution of the Hanford Formation, determined during characterization testing, was used to design and proportion the surrogate test soil. Local aggregate sources in New Jersey were sampled to identify and obtain the components of the surrogate soil. Aggregate sources were selected considering size, sphericity, roundness, tenacity, organic content, and gross mineralogy in an attempt to simulate the Hanford Formation soil as closely as possible. The gravels and cobbles were washed to

Table 3.1 Comparison of Physical Data-Hanford Soil and Surrogate Test Soil

Test	Method	Parameter	Hanford Soil	Surrogate Soil*
Grain Size Analysis:	ASTM D 2217-85	cobbles	22.3 wt%	25 wt%
Washing (No. 200 sieve),	ASTM D 1140-92	gravels	27.6 wt%	30.7 wt%
Manual Separation,	ASTM D 422-63	sand	46.7 wt%	40.9 wt%
Mechanical Sieve,		silt	3.3 wt%	2.7 wt%
and Hydrometer Test		clay	0.1 wt%	0.7 wt%
Liquid and Plastic Limits	ASTM D 2217-85 ASTM D 4318-84		Non-plastic	Non-plastic
Organic Content	ASTM D 854-92		0.12 wt%	0.28 wt%
Specific Gravity	ASTM D 854-92		2.82	2.66
USCS Classification	ASTM D 2487-93		GP	GP
Color	Munsell® Soil Color Charts (air dry soil)		Batch 1--10YR 5/6: Yellowish Brown Batch 2--10YR 4/2: Dark Grayish Brown	2.5Y 6/4: Light Yellowish Brown

*   Sample for grain size analysis was collected after 12 fracture sessions; sample is not 100% representative of original blend.
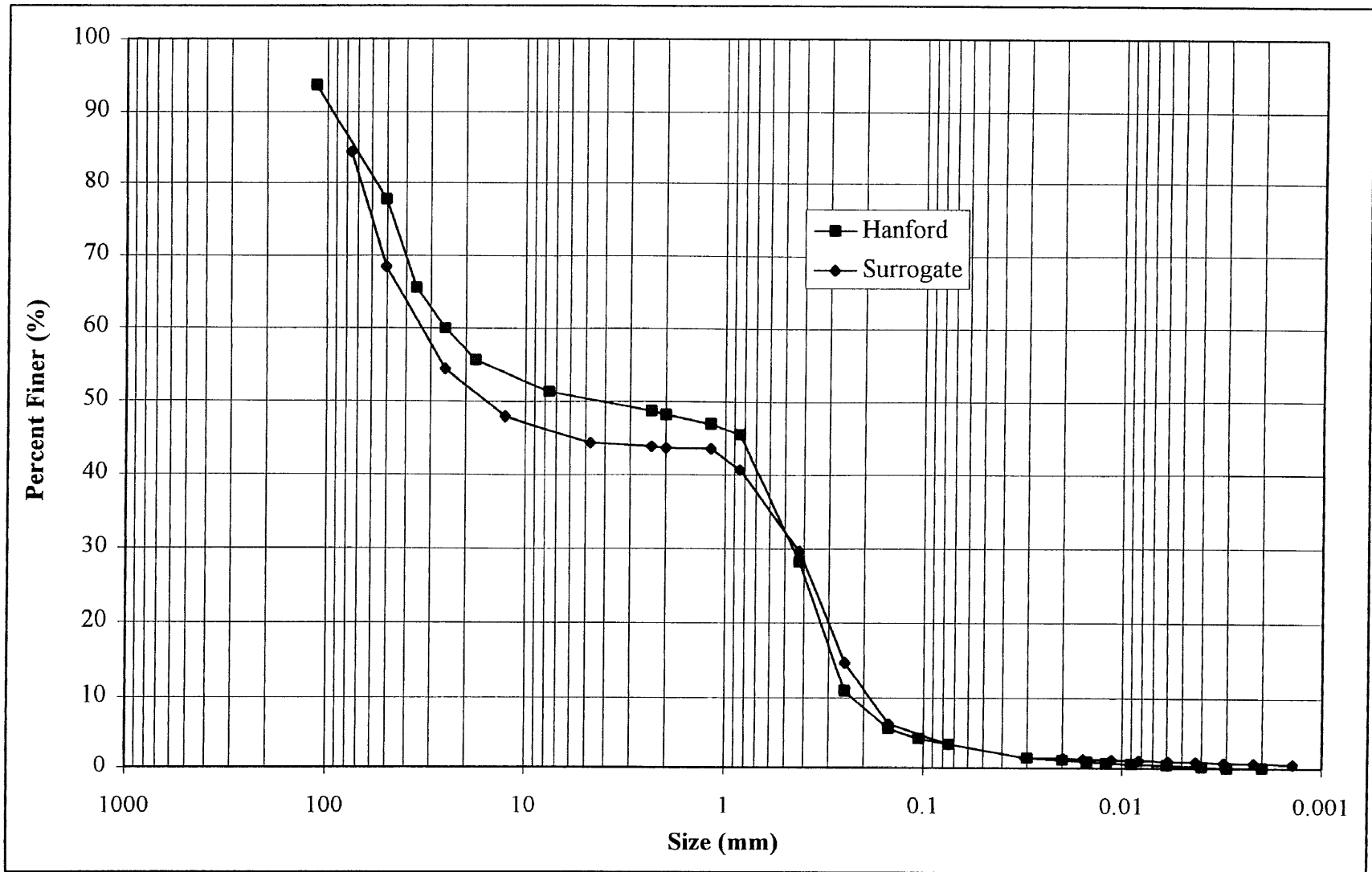
Figure 3.1 Grain Size Comparison of Hanford and Surrogate Test Soils

remove fines and hand picked to remove angular-shaped specimens. The aggregate sources were then separated into the 16 fractions using a mechanical sieve for the sands and gravels, and manual separation for the cobbles. Due to the large amount of soil needed for the bench scale study and the fast track nature of the project, a high capacity mechanical sieve was used to process the aggregates. The required weight of each fraction was calculated using the appropriate design proportion. The fractions were then placed into a large mixing tub, and mixed by hand to create a uniform soil.

3.1.3 Verification of Surrogate Test Soil Compatibility

Laboratory tests were performed on the surrogate test soil to verify compatibility with the Hanford Formation soil. The same testing procedures were followed for both the surrogate test soil and the Hanford Formation soil previously discussed in Section 3.1.1. The results of these tests are presented in Table 3.1 and Figure 3.1, which also contain the results of the Hanford Formation soil for comparison purposes. As indicated, the prepared surrogate was similar to the parent Hanford soil. The surrogate test soil had a slightly higher gravel-cobble content, but this was attributed to the loss of sands during fracturing and excavation, as the grain size analysis on the surrogate test soil was performed after twelve tests were completed.

The most significant incompatibility between the surrogate test soil and the Hanford Formation soil was specific gravity. The specific gravity of the surrogate soil (2.66) was lower than the specific gravity of the Hanford Formation soil (2.81), which

reflects the higher quartz content (Gs of quartz = 2.65) of the surrogate test soil. Thus, the overburden weight of Hanford Formation soil at a given depth would be 5.6% greater than an equivalent thickness of surrogate test soil. This difference was not expected to have a significant effect on the test results, since the overburden weight applied during bench scale testing was only 20% of the overburden weight which will be present in the field.

3.2 Tank Tests

A series of tank tests were performed to simulate the in situ conditions of the pneumatic fracturing process using a small scale environment. This section will detail the experimental set up and procedure of the fracture tank test activities. The surrogate test soil, described in the previous section, was used exclusively for these experiments. The overall objective of these tests was to investigate the fracture mechanisms of the surrogate test soil, both quantitatively and qualitatively.

3.2.1 Experimental Set Up

The set up of the fracture test tank study consisted of the fracture test tank, an air supply system, a flow directing injector-nozzle and a venting system. Also, a dry media injection system was utilized for some of the experiments. A schematic cross section of the fracture test tank is provided in Figure 3.2. The fracture test tanks were constructed from Plexiglas to view the results of each injection directly, and to permit real-time
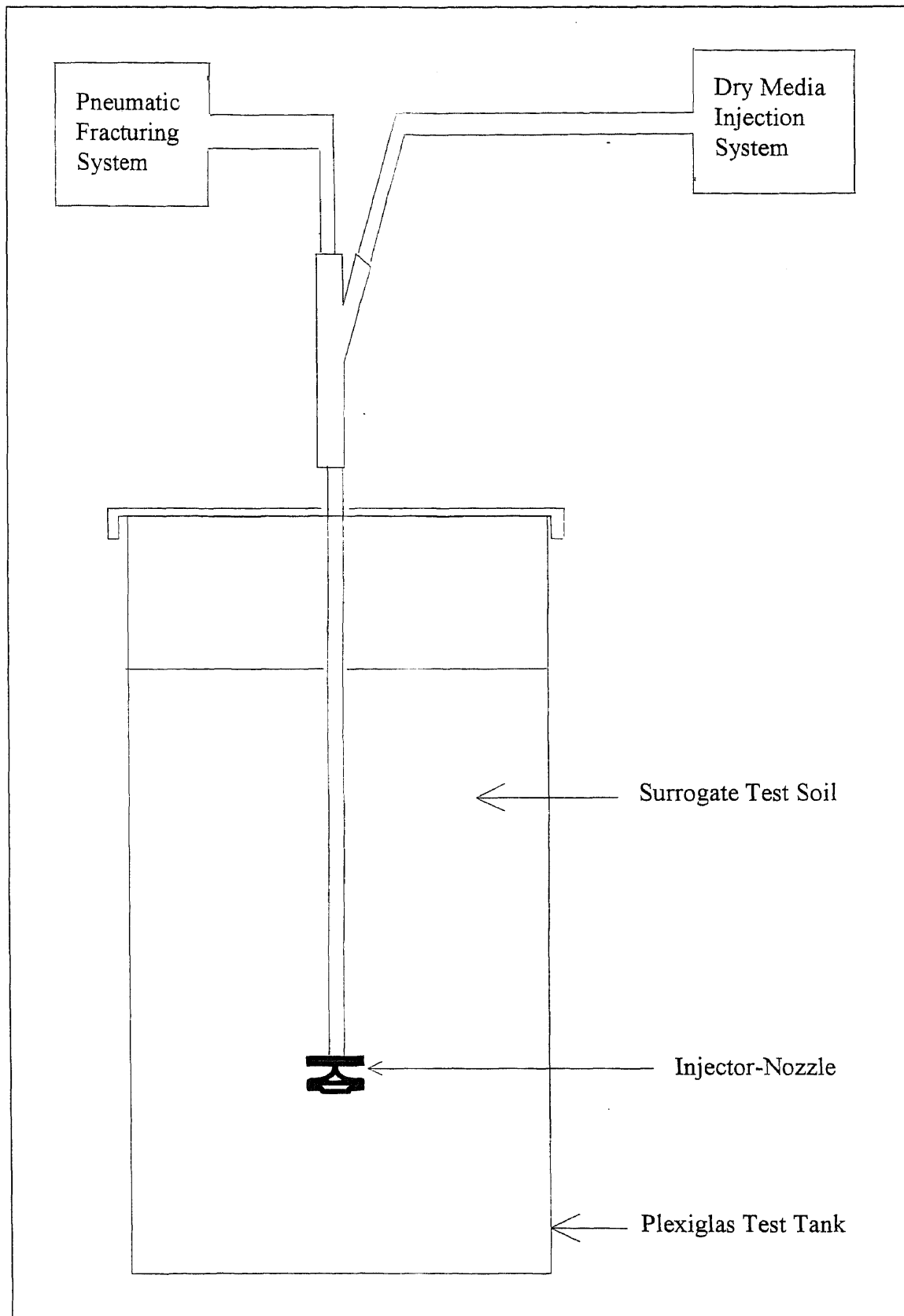
Figure 3.2   Schematic Diagram of Fracture Test System

adjustment of injection pressures and flows during the test. The tanks measured 1.21 ft

(0.4 m) by 1.21 ft (0.4 m) by 3.34 ft (1.0 m) high and had a volume of 4.9 ft^3 (0.14 m^3).

Two separate air supply systems were used for the fracture test tank studies. The

majority of the tests were performed in the laboratory using centralized compressed air at

a line pressure of 120 psi (828 kPa). System control was provided by a regulator, a 16

ft^3 (0.45 m^3) capacity surge tank and a remote actuated valve. Tank tests involving

graphite/glass frit injection were performed outside to minimize the inhalation hazard

and to prevent contamination of equipment. These tests were performed using the full

scale PF trailer, although only four of the trailer's twelve air cylinders were needed due to

the limited duration of the tests.

The injector-nozzle consisted of a 1 in. (25.4 mm) diameter pipe (nominal)

equipped with a basic conical nozzle which directed air radially into the soil through four

0.5 in. (12.7 mm) diameter holes. Several different nozzle designs were tried during the

first ten tests, at which time the design was finalized for the remaining tests. The most

successful design consisted of two 4 in. (10.2 cm) diameter discs spaced 0.125 in. (0.32

cm) apart. This nozzle design directed the flow radially, and also helped limit air escape

along the injector pipe.

Initially, dry media injection was accomplished with a modified 80 lb (36.3 kg)

sandblaster which was attached to the injection pipe in a "Y" configuration. This set up

enabled the simultaneous injection of the dry media and the primary injection air. Flow

and pressure of the dry media system was controlled independently. A second system

was developed to inject the dry media, which is shown schematically in Figure 3.3. The

Direction of
Air Flow

1 1/2"

Select Pre - By Pass Valve
or Post - By Pass Valve

1 1/2" Y

To Borehole

2" Y

1"

T

Tube Truck
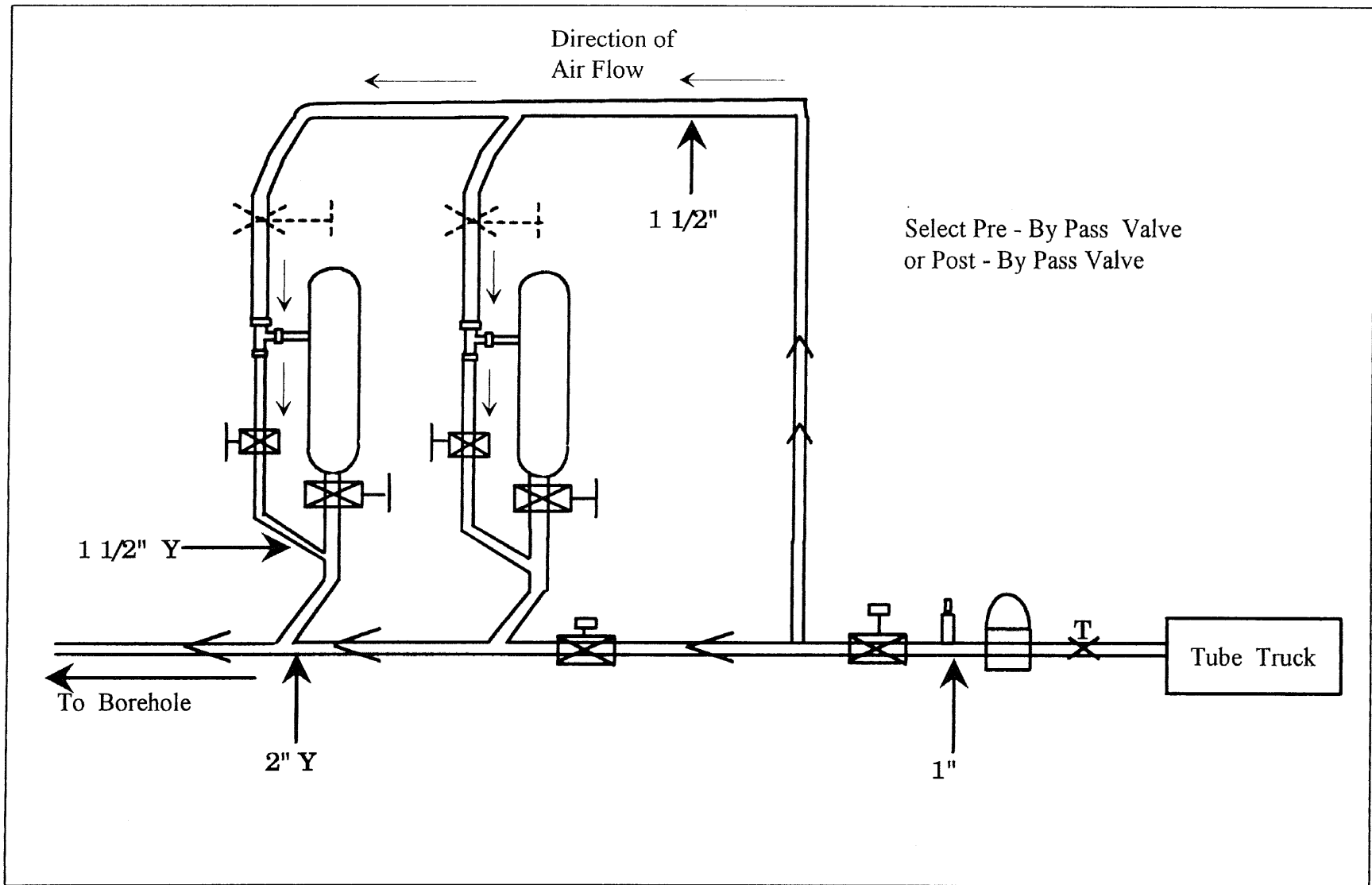
Figure 3.3 Dry Media In Line Injection System

system utilized a single air stream to produce the fracture, energize the dry media, and transport the dry media into the fracture. This will be referred to as the in line dry media injection system.

3.2.2 Experimental Procedure

Test tank preparation began with the determination of the moisture content of the surrogate test soil. The moisture content of the soil was calculated using the direct heating method described in ASTM D 4959 (1994). If the moisture content was found to be lower than desired, the quantity of water required to raise the moisture content to the desired level was added to each lift prior to packing. Periodically, ASTM D 2216 (1994) was used to calculate the moisture content to check the results against those determined using the direct heating method. This method produced results approximately 0.5 to 1.5 wt% lower than the first method. Therefore, the moisture contents are possibly biased high. For these tests, soil moisture ranged from 0.8 to 7.8 percent by weight.

Vent wells were installed in each corner of the tank during packing to reduce pressure build-up in the tank and to simulate radial dispersion of air into the formation. The vent wells consisted of 0.5 in. (1.27 cm) PVC slotted pipe, and were installed to the bottom of the tank.

Dry density was varied from 103-112 lb/ft^3 (1.65-1.80 g/cm^3) in order to study the effect of dry density on the ability to create and control a fracture. Density control was maintained by weighing the soil in each lift with appropriate adjustment for moisture content. Once the soil was placed in the tank and the cobbles were oriented roughly

horizontal, the lift was compacted to the proper level. To achieve a uniform dry density throughout the tank, the soil was packed in 3 in. (76.2 mm) lifts. The injector-nozzle was placed on the top of the third lift in the center of the tank. It is noted that no compaction was needed to achieve a dry density of 103 lb/ft^3, which is expected to be the lower range of natural bulk density of the Hanford Formation (Bjornstad and Murphy, 1994).

Of the forty-four tank tests performed, surcharges were applied to the top of the soil beginning with fracture test tank no. 16, and to all subsequent sessions in an effort to better simulate overburden in the field. Even with the added surcharge, the overburden in the bench scale study was only 20% of that expected in the field.

Once the tank was packed, the air supply system was connected to the injector pipe by a 1 in. (25.4 mm) diameter hose. The initial pressure was adjusted until a discrete fracture was formed. If no fracturing occurred and the soil was not ejected out of the tank, the pressure was increased. If rapid fracturing occurred upwards through the formation, the pressure was reduced for the next test run.

Out of the forty-four tank tests performed, thirty-four of the tests involved air injection exclusively, while ten of the experiments involved injection of both air and dry media. Of the dry media tests, six utilized silica sand and four utilized a graphite/glass frit mixture. For these experiments, the initial pressure in the sandblaster ranged from 18-21 psi (124.2-145 kPa). The sandblaster flow rate was controlled manually and the media injection commenced once a fracture had been created. Injection of dry media was continued until a continuous lens was created, or until the media was ejected from

the test tank. Some injections using the in line dry media injection system were terminated when the canister was emptied, since this system had a smaller media capacity.

3.3 Conductivity Tests

Conductivity tests were performed on four test tanks following injection of graphite/glass frit. These tests simulated the integrated PF/ISV process most closely, since they permitted verification of electrical conductivity between electrodes. The number of conductivity tests were limited to four to reduce the volume of surrogate soil needed for the tests, since the graphite/glass frit contaminated the surrogate test soil and rendered it unusable for further tests.

3.3.1 Experimental Set Up

The test tanks for the conductivity tests were prepared as previously described for the test tank experiments, except electrodes were also installed to facilitate conductivity measurements. Initially, two 1.5 in. (38.1 mm) diameter by 2 ft (0.61 m) cylindrical electrodes, composed of graphite with a molybdenum core (Superior Graphite Co., Chicago, IL), were installed spaced 12 in. (0.30 m) apart beginning at nozzle level and extending to the soil surface. These are the same electrodes that are used in ISV engineering scale tests, where they are spaced about 1 m (3.3 ft) apart. To better simulate scale and to enable the test tank to be more uniformly compacted, smaller

aluminum electrodes with a diameter 0.5 in. (12.7 mm) were used in the final conductivity experiment.

3.3.2 Experimental Procedure

The electrical conductivity of the injected lens was determined by applying a variable voltage source across the electrodes and measuring the resulting current. A schematic of the conductivity test set up is shown in Figure 3.4. Measurements were taken before and after injection of the graphite/glass frit at three different voltage levels to evaluate changes in conductivity. The voltage was applied to the system by a Powerstat Variable Transformer (Superior Electric Co., Inc.) and measured by a Fluke 8050A digital voltmeter (John Fluke Manufacturing Co.). The induced current in the system was then measured by a Fluke 85 ammeter (John Fluke Manufacturing Co.). To minimize the inhalation hazard and to prevent contamination of laboratory equipment, tests involving graphite and glass frit were performed outdoors in the parking lot of the CEES Laboratories.

The graphite/glass frit mixture for the bench scale tests consisted of a 50/50 proportion by weight of graphite (1501 natural crystalline flake-80% minimum retained on No. 50 sieve) and glass frit (85% passing No. 200 sieve). The grain size distributions are shown in Appendix E. This is the same starter path mixture utilized by Battelle to initiate vitrification melts.
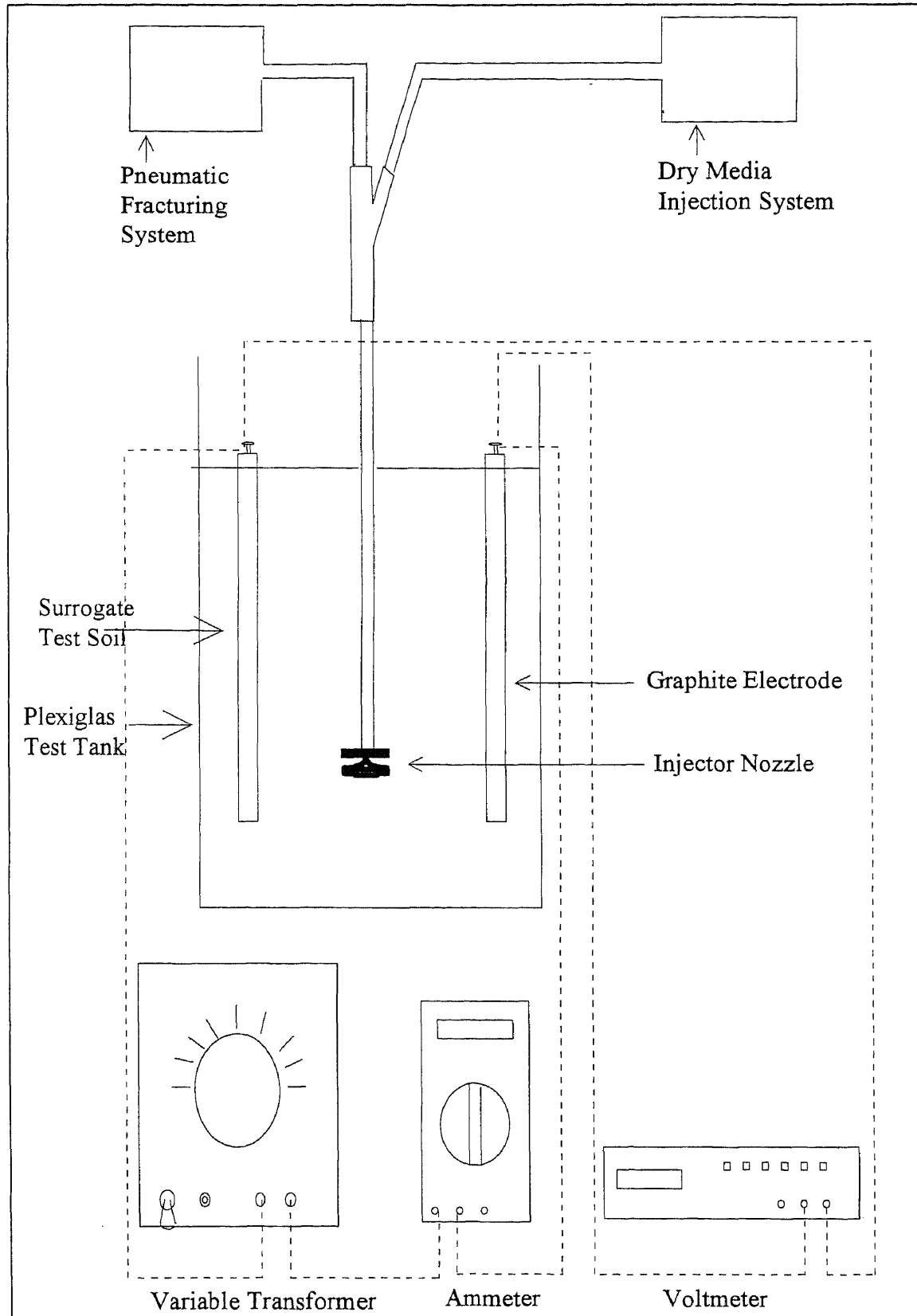
Figure 3.4 Conductivity Test Schematic

3.4 Horizontal Infiltrometer

Horizontal infiltrometer tests were conducted to investigate whether interstitial transport of the graphite/glass frit mixture alone can be relied on to create a conductive plane. Interstitial transport may also be a significant factor in extending the conductive lens beyond the reach of a discrete fracture.

3.4.1 Experimental Set Up

As shown in Figure 3.5, the experimental apparatus consisted of a Proctor mold, in which the soil was compacted to the desired density and moisture content. The Proctor mold was closed at both ends using 'O' rings and end plates, and was then sealed tightly by tie rods and nuts passing through the end plates. Air flow was induced through the soil by applying a pressure differential controlled by a pressure regulator and a ball valve. The pressure differential and flow rate were measured using a Bourdon tube pressure gauge and a set of rotameters. A graphite injection port was provided at the upstream end of the mold.

3.4.2 Experimental Procedure

First, the soil was compacted in three layers with 25 blows per layer using the standard Proctor compaction rammer. The apparatus was assembled and pressure tested for air tightness before the beginning of each experiment. After pressurization, dry media was introduced into the system in four separate slugs. After introducing each slug into the
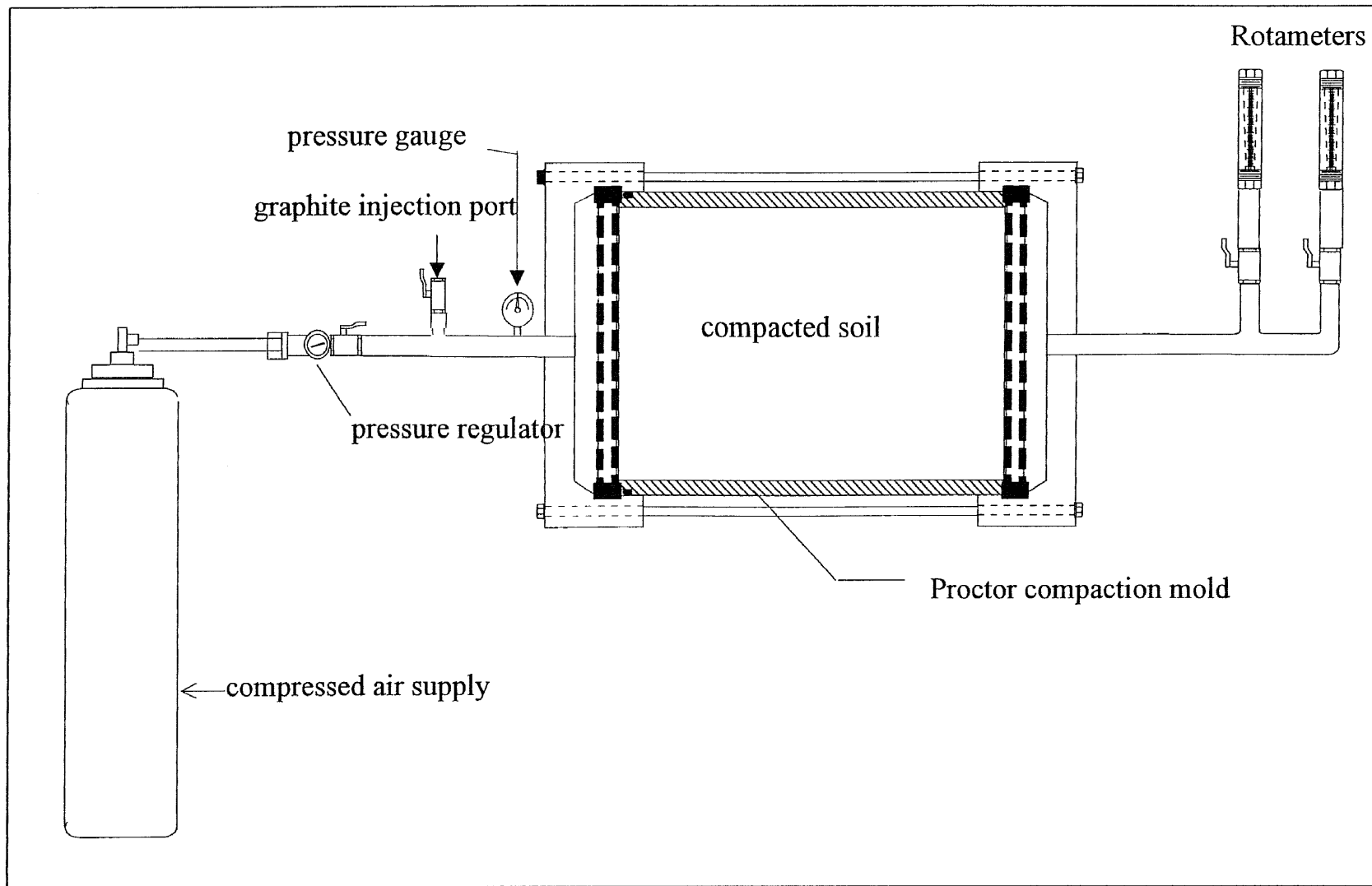
Figure 3.5 Graphite Infiltration Test Schematic

port, airflow was increased gradually to fluidize the media and carry it downstream. A flow of 5 cfm (39 cm^3/min) was maintained for the injection of each slug.

During all the experimental runs, particles collected on the porous media, thereby decreasing the permeability. Under constant pneumatic head, permeability reduction was measured as a decrease in flow rate. At constant flow rate, permeability reduction was indicated by increased pneumatic gradient. Hence, to observe any changes in permeability after the injection of the last slug, the pressure or flow was fixed at the desired value according to which parameter needed to be measured.

Soil type, media mixture, moisture content, and injection pressures were varied throughout the experiments. Tests were performed on three different soil variations: soil passing sieve No. 8; soil passing sieve No. 8 with a cobble placed at the inlet end; and 50% soil passing sieve No. 8 mixed with 50% gravel ranging in size from 0.4-1 in. (1.0-2.5 cm) in diameter. Four different types of dry media were injected: 50% graphite (1501) and 50% glass frit mixture; graphite 205; graphite 635; and glass frit. These materials are described in Appendix E. Two different moisture content ranges were used: 5-6 wt% and 2-3 wt%. Two differential injection pressures were used: 4 psi (27 kPa) and 35 psi (242 kPa).

3.5 Segregation Tests

An area of concern in the PF/ISV process is the potential for segregation of the graphite/glass frit particles during dry media injection. If the graphite and glass frit are not sufficiently integrated, the melt may not initiate. Some simple bench scale tests were

performed to address the question of segregation in the PF/ISV system in light of analytical modeling results in Section 5.2. First, based solely on theoretical settling velocities, the glass frit might be expected to travel farther than the graphite. Second, the results of one of the transport models showed some variance in the critical suspension velocities for deposition from the air stream.

3.5.1 Experimental Set Up

The tests used a 9.7 ft long (3 m) by 3.25 in. (8.25 cm) diameter butyrate tube oriented horizontally to contain the graphite/glass frit mixture as it was injected into the tube. The tube was equipped with a filter at the output end, which allowed air to escape, but retain a majority of the dry media. The injector-nozzle of the PF system was simulated by placing a disc with a rectangular slot 0.3 in. (0.8 cm) by 1.0 in. (2.5 cm) at the entrance of the tube.

3.5.2 Experimental Procedure

Tests were performed by using four air cylinders from the full scale PF system and the in line dry media injection system to inject 6 lb (2.72 kg) of graphite/glass frit mixture at a pressure of 30 psi (183 kPa). Since the experimental butyrate tube was transparent, visual observations were possible both during injection and upon completion. The tests were terminated when it appeared that the dry media had been exhausted.

CHAPTER 4

LABORATORY RESULTS

This chapter presents and discusses the results of the laboratory tests. The results of the most extensive study, the fracture test tank study, are presented in Section 4.1. The conductivity test results, which stem from the injection of graphite/glass frit into the fracture test tank, are discussed in Section 4.2. The results of horizontal infiltrometer tests are described in Section 4.3, while segregation test results are presented in Section 4.4.

4.1 Fracture Test Tank Results

A total of forty-four tank tests were performed during the fracture test tank study. The experimental parameters for each of the tank tests are summarized in Table 4.1, along with brief observations made during each test. The remainder of this section discusses the effects of a number of experimental parameters on the fracture behavior of the surrogate test soil including: 1) density effects; 2) moisture effects; 3) nozzle design; 4) wall effects; 5) refracture behavior; 6) aperture control; 7) fracture inclination; and 8) lens formation.

4.1.1 Effect of Density

The most important factor affecting the fracture behavior of the surrogate test soil was density. Generally, fracture injections made above a dry density of 105 lb/ft^3 (1.68

Table 4.1 Summary Table of Fracture Sessions

Fracture Test Tank No.	Date	Moisture (wt %)	Dry Density (lb/ft^3)	Injection Pressure (psi)	Injector Type	Remarks
1	5/24/94	6.6	103	15	A	Air escaping around injector & along walls.
2	5/27/94	3.1	103	31	B	Fractured @ 12 in(15°), 2 in aperture
3	5/31/94	4.06[1]	103	35	C	Fractured momentarily then vertical fractures
4	6/1/94	3.34[2]	103	36	C	Fractured momentarily then vertical fractures
5	6/3/94	3.5	103	30	D	Fractured at several levels
6	6/3/94	5.6	108	32	C	Fractured @ 12 in(15°), closed w/ decreased flow
7	6/6/94	7.8	112	30	C	Fractured @ 12 in(15°), closed w/ decreased flow
8	6/6/94	7.03	112.8	18	C	No discrete fractures
9	6/7/94	6.77	112	35	E	Fractured momentarily then vertical fractures
10	6/7/94	6.77	112	35	F	Fractured @ 13-14 in(22-29°),but too much pressure blew soil out of tank
11	6/7/94	6.77	112	30	G	Fracture @ 15 in (35°)& held
12	6/7/94	6.77	112	30	G	Fractured momentarily then vertical fractures
13	6/7/94	6.77	112	30/20[4]	G	Fracture @ 15 in(35°) & held
14	6/9/94	5.2	112	25	G	Fractured momentarily then vertical fractures
15 **	6/9/94	6.0	112	25	G	Frac. @ 15 in(35°), 1 in aperture, sand inj. for 7 minutes to comp. fill frac.
16	6/13/94	6.0	112	25	G	Fractured at several levels, surcharge = 80 lb.
17 **	6/13/94	5.2	112	25/23[3]	G	Fracture @ 14 in(29°), sand inj. @ 19 psi, 1 in sand lens, surcharge-80 lb.
18 *	6/14/94	5.5	112	200/70[3]	G	Initial frac.-14 in(29°), then 18 in, g/g frit injected @ 20 psi, conductive lens, surcharge = 80 lb

Table 4.1 (continued) Summary Table of Fracture Sessions

Fracture Test Tank No.	Date	Moisture (wt %)	Dry Density (lb/ft³)	Injection Pressure (psi)	Injector Type	Remarks
19*	6/14/94	5.5	112	100/170[4]	G	Frac. @ 14 in(29°), g/g frit inj. @ 20 psi lens not conductive, surcharge = 80 lb
20	6/29/94	1.0	110	38/29[3]	G	1 in frac. aperture., duration-5+ min., surcharge = 92 lb
21	6/29/94	2.0	110	35/25[3]	G	Frac. @ 14 in(29°), aperture = 2-6 in, duration-8+ min., frac. re-opened @ 15 in, surcharge = 92 lb
22	6/29/94	3.3	103	35	G	A discrete frac. wasn't seen, pockets of separation & 1 in levitation seen, surcharge = 92 lb
23	6/29/94	3.3	103	37.5/29[3]	G	Frac. @ 14-15 in(29-35°), aperture 4-6 in, continuous fracture, surcharge = 92 lb
24	6/29/94	0.8	107	35	G	Fractured momentarily then vertical fractures, surcharge = 92 lb
25**	6/30/94	2.0	110	35	G	Frac. @ 13 in(22°), aperture 4-6 in, sand inj. @ 29 psi, lens-2.5 in avg., surcharge = 92 lb
26	7/5/94	1.0	103	43	G	Did not fracture as air escaped by following cobble path along vent pipes; surcharge-92 lb
27 **	7/5/94	1.0	103	41	G	Fractured and began sand injection, but aborted due severe sand losses from tank; surcharge-92 lb
28	7/5/94	1.0	103	39	G	Visible air pockets in formation noticed prior to frac., air escaped along these pockets, surcharge = 92 lb
29	7/6/94	1.0	103	40	G	Soil heaved about 1 in, but no discrete fracture, surcharge = 92 lb
30	7/6/94	1.0	103	46	G	Frac. @ 12 in, but not able to hold, surcharge = 92 lb

Table 4.1 (continued) Summary Table of Fracture Sessions

Fracture Test Tank No.	Date	Moisture (wt %)	Dry Density (lb/ft^3)	Injection Pressure (psi)	Injector Type	Remarks
31	7/6/94	1.0	103	42	G	Visible air pockets in formation noticed prior to frac., air escaped along these pockets, surcharge = 92 lb
32	7/7/94	1.5	105	----	G	A hairline fracture started @ 9 in, then a discrete fracture @18 in, followed by escape of air, surcharge = 92 lb
33	7/7/94	1.5	105	----	G	Initial movement @ 9 in, then fractured @ 12-14 in(15-29°), but could not hold
34 **	7/7/94	1.5	105	----	G	Crack @ 12 in(15°), sand injection @ 9-12 in, continuous lens avg. thickness- 3 in
35 *	7/8/94	1.5	105	70/60^3	G	Frac. @ 9 in, injected non-conductive layer due to escape along injector
36**	8/5/94	3.0	105	-----	G	Fracture sustained on third attempt at 24 in due to re-compaction of the top layers after two non-sustained fractures, aperture=1 in, successful sand injection
37	8/8/94	3.0	105	-----	G	Fracture @ 12 in at wall, but not held due to too much pressure then decreased too quickly
38 *	8/9/94	3.0	105.5	23	G	Fracture @ 13 in at wall, graphite inj., conductive layer measured w/Al electrodes, re-opened fracture twice
39	10/27/94	2.75	103	55/45^3	G	Fracture initiated at 13" and after several seconds soil collapsed, refracture was sustained at 21".

Table 4.1 (continued) Summary Table of Fracture Sessions

Fracture Test Tank No.	Date	Moisture (wt %)	Dry Density (lb/ft^3)	Injection Pressure (psi)	Injector Type	Remarks
40	10/28/94	2.75	107	45/50/35[5]	G	Fractured at 15" initially, some soil collapsed as the fracture was increased. Fracture then held at 18"
41	11/4/94	2.75	111	41	G	Fracture initiated at 13"; maintenance pressure equaled initiation pressure.
42	1/10/95	1.5	107	47	G	Fracture initiated at 12"; maintenance pressure equaled initiation pressure.
43	1/13/95	2.5	107	47	G	Fracture initiated at 12"; maintenance pressure equaled initiation pressure.
44	1/16/95	3.5	107	48	G	Fracture initiated at 15"; maintenance pressure equaled initiation pressure.

* Graphite/Glass frit injection

** Sand injection

[1] The moisture content shown was taken before the fracture, but a moisture content of 4.7% was found after fracture.

[2] The moisture content shown was taken before the fracture, but a moisture content of 4.86% was found after fracture.

[3] The first pressure is the pressure to open fracture; the second pressure is the pressure to sustain fracture.

[4] The first pressure opened fracture momentarily; second pressure needed to reopen fracture, but started to push soil out of tank.

[5] The first pressure created slight fracture; the second pressure increased fracture aperture; third pressure is the maintenance pressure.

A-Pipe with four 0.5" diameter holes

B-A 6" plastic disc loosely attached above the nozzle to create a seal around the injector and direct flow

C-Same as B, but fixed at 12" height with collar

D-A 6" plastic disc designed to slide along injector pipe and still create a seal

E-Reduced the four 0.5" holes to 1/8" slits by using collars to cover most of the hole

F-Same as E, but collars has 1/4" flange

G-Same as E, but collars has 4" flange

g/cm^3) were successful, while inconsistencies were observed at lower densities. A few

fractures were initiated at a density as low as 103 lb/ft^3 (1.65 g/cm^3), although these

occurred only at higher moisture contents. It was not possible to initiate successful

fractures with the combination of low density and low moisture content.

Figure 4.1 illustrates the relationship between fracture pressure and density for

the successful fractures obtained using the laboratory air injection system with and

without a surcharge load. As density was increased, the pressure required to initiate

fracturing tended to decrease. The addition of a surcharge to the top of the soil appeared

to accentuate this effect, as indicated by the higher slope for the surcharge data. The

trend due to the addition of the surcharge is significant, and suggests that higher

pressures will be needed to account for the expected field overburden. The fracture

initiation pressure recorded in these tests was measured in the supply tank, so the actual

fracture initiation pressure was slightly less. Note that the moisture content was varied

during these tests.

To confirm the density-pressure trend observed in test nos. 1-38, three additional

tests were conducted at a constant moisture content. The dry densities chosen were 103,

107 and 111 lb/ft^3 (1.65, 1.71, and 1.78 g/cm^3) at a moisture content of 2.75 wt%. The

full scale PF system was used for these tests since it allowed better pressure control and

greater accuracy. The relationship between fracture pressure and density for the full

scale system is shown in Figure 4.2. The pressures plotted for these tests were taken

from the regulator gauge, which is located just before the test tank. Although the
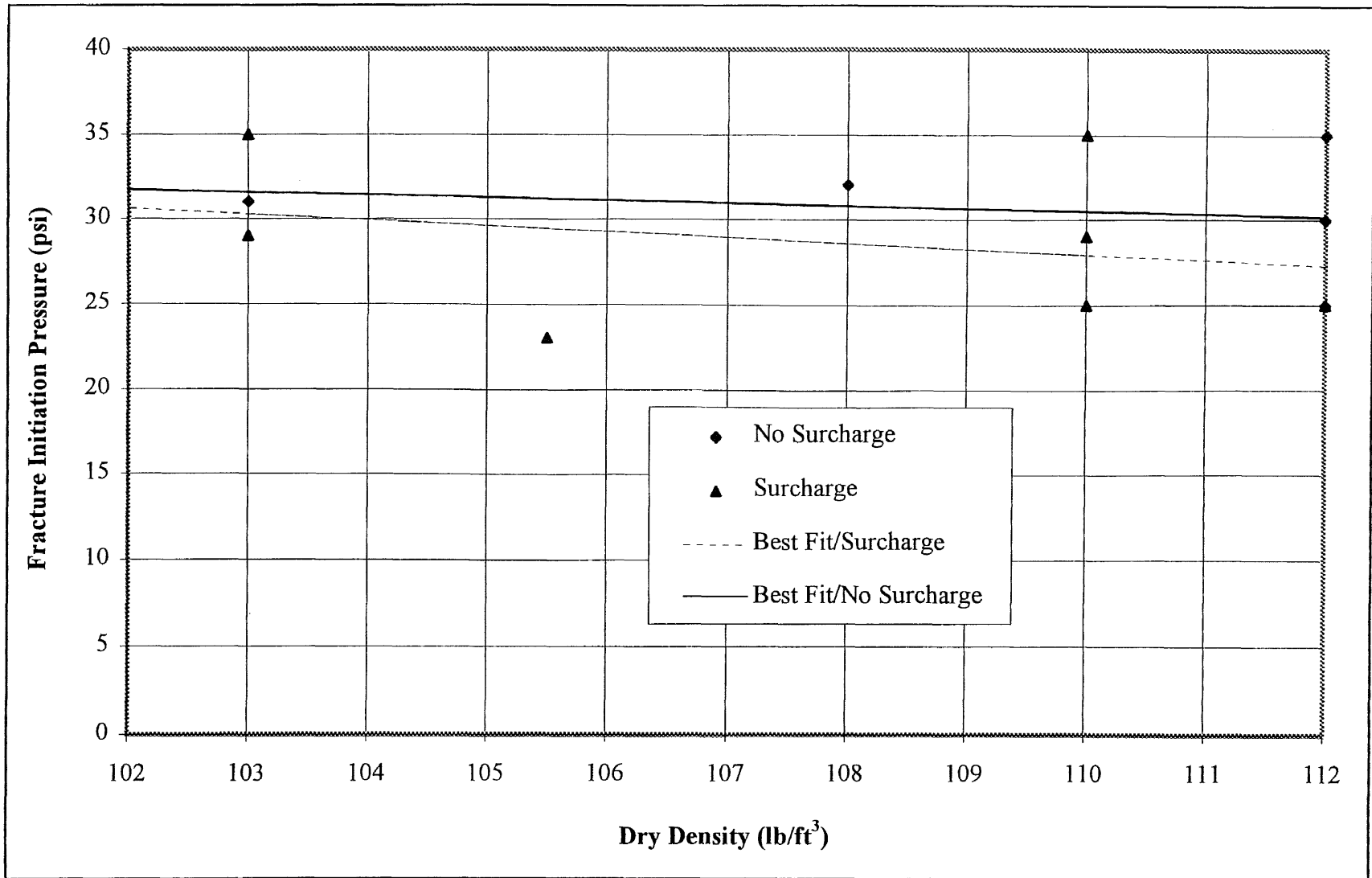
Figure 4.1 Fracture Initiation Pressure vs. Dry Density
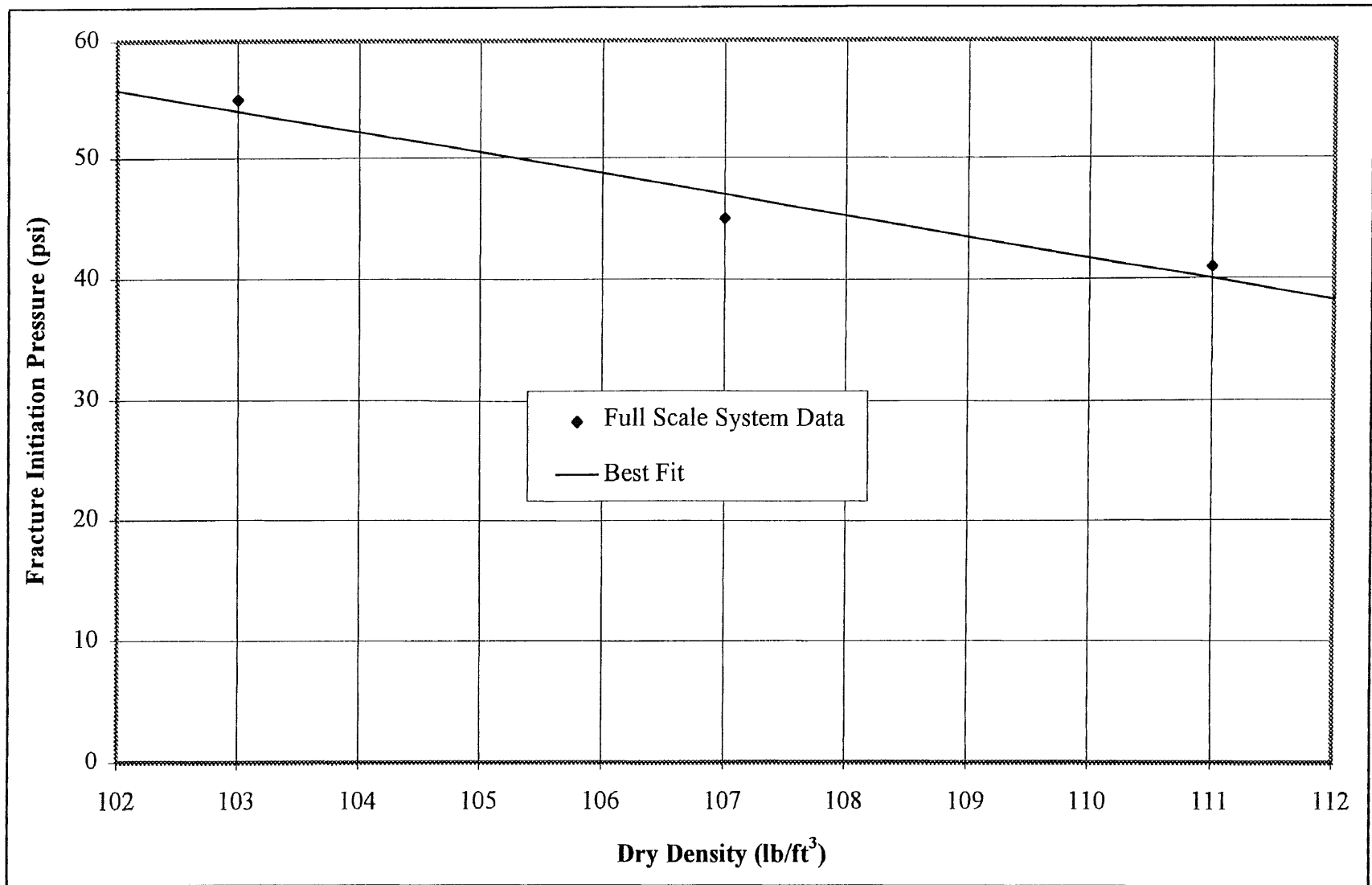
Figure 4.2 Fracture Initiation Pressure vs. Dry Density Using Full Scale System

magnitude of the initiation pressure increased slightly due to system differences, the inverse trend between density and pressure was confirmed.

4.1.2 Effect of Moisture

Moisture was also determined to have a significant effect on the ability to pneumatically fracture the surrogate test soil. Fracturing was generally successful at moisture contents exceeding 2 wt%. Fracturing at lower moisture contents was successful only for relatively high densities (105-112 lb/ft^3 (1.68-1.79 g/cm^3)). At densities equal to or below 103 lb/ft^3 (1.65 g/m^3), which is the expected lower density range of the Hanford Formation soil at the ISV test site, a discrete fracture below 1 wt% moisture was unattainable.

Data showing the effect of moisture content on fracture initiation pressure are presented in Figure 4.3. Initially, it was expected that the fracture pressure might decrease as moisture content increased, due to the effects of apparent cohesion and the "sealing" effects of interstitial moisture. A review of the data show a mixed result, however, with constant pressure for no surcharge and a declining pressure for surcharge tests. Note that the dry density was varied in these tests.

To further investigate this relationship, three additional tests of variable moisture content (1.5, 2.5, and 3.5 wt %) were performed using the full scale PF system at a constant dry density of 107 lb/ft^3 (1.71 g/cm^3). The relationship between fracture initiation pressure and moisture content for these tests is illustrated in Figure 4.4. The
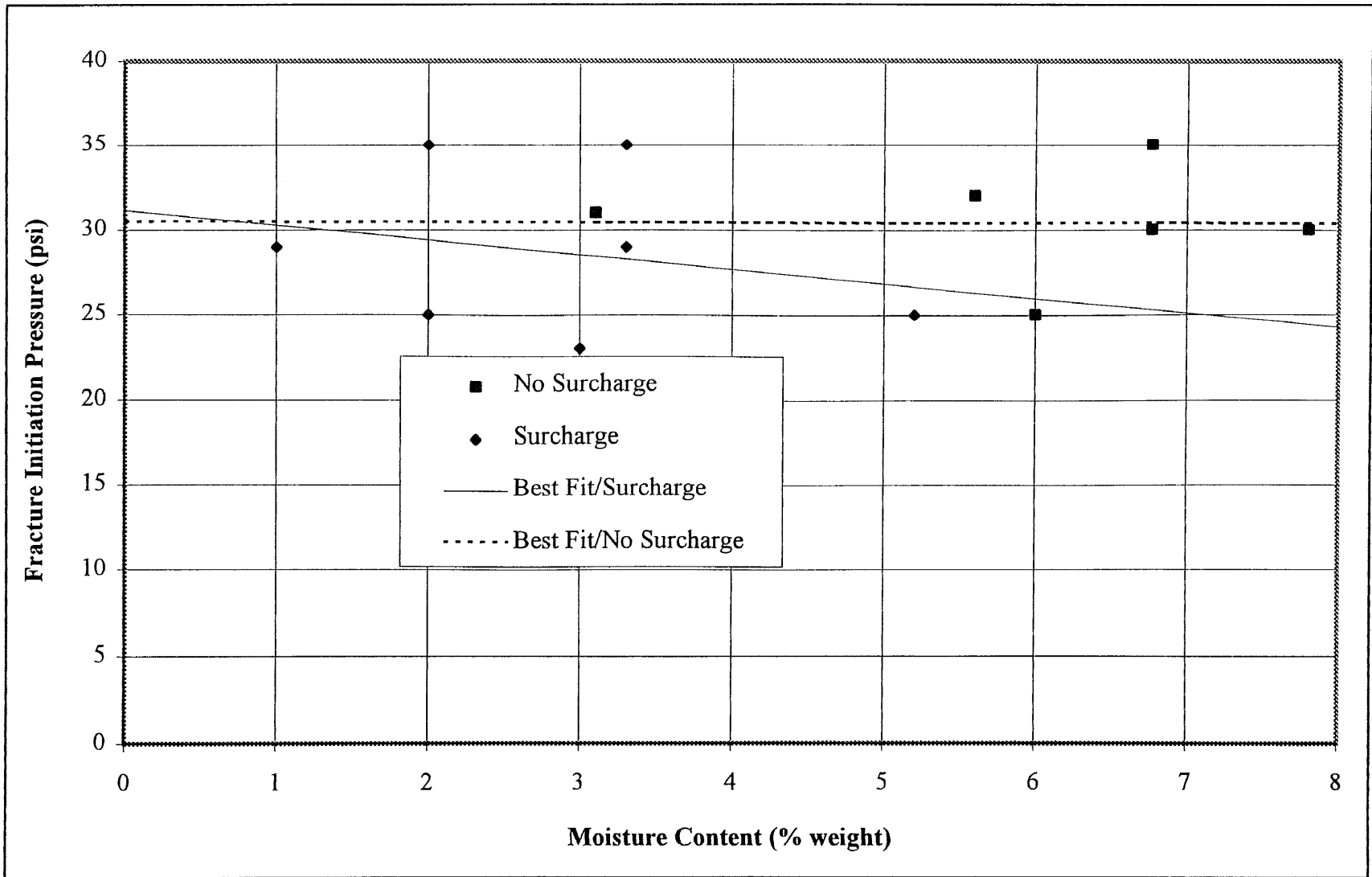
Figure 4.3 Fracture Initiation Pressure vs. Moisture Content
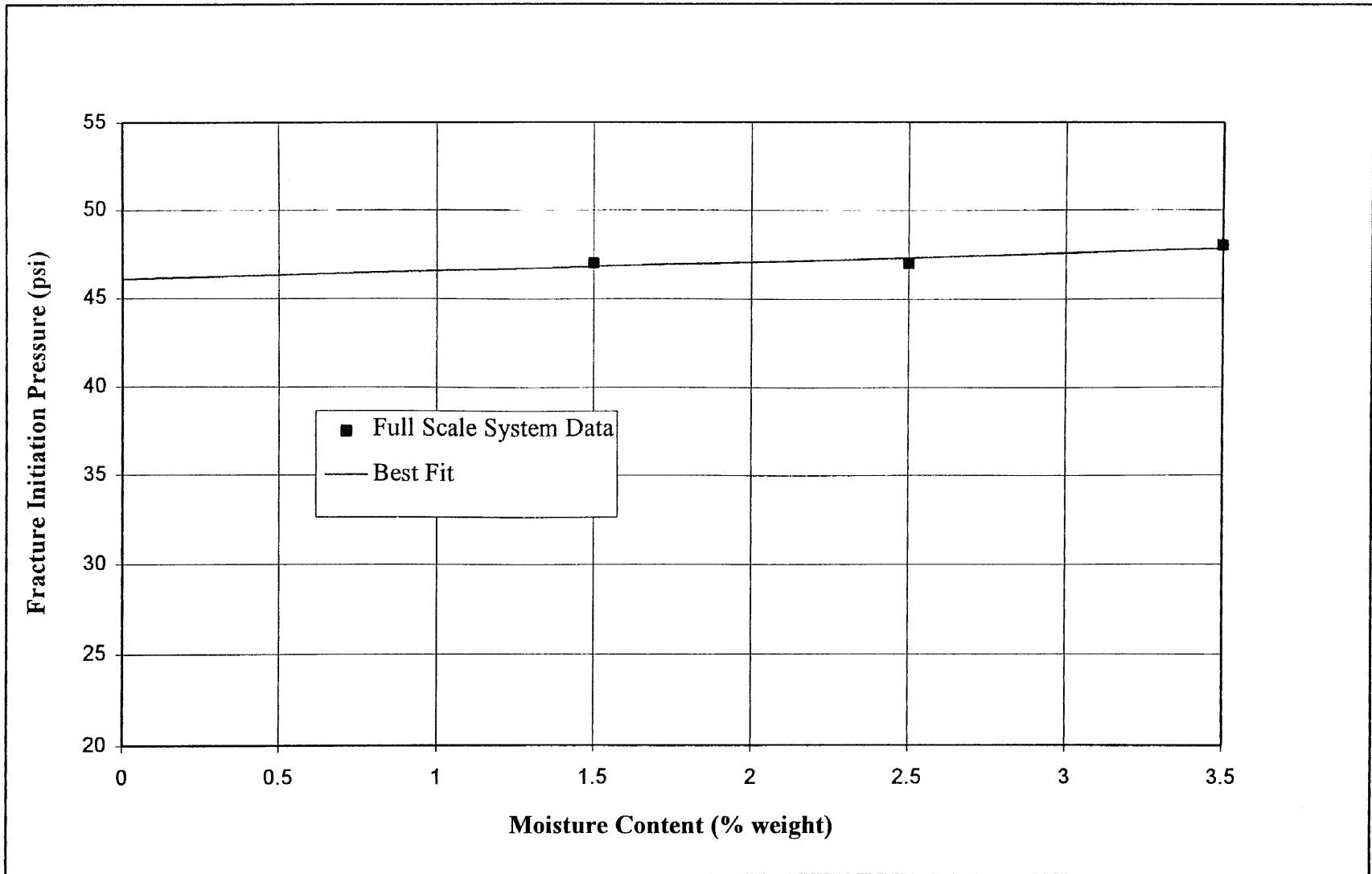
Figure 4.4 Fracture Initiation Pressure vs. Moisture Content Using Full Scale System

slope of the data using the full scale system match the trend of the "No Surcharge" tests using the laboratory scale system, even though a surcharge was used for the additional tests. A review of the overall test results on moisture effects suggest several tentative conclusions. At very low moisture contents, below 1 wt% moisture, there is insufficient moisture to provide interstitial surface tension and the resulting apparent cohesion. However, above 1 to 1.5 wt% moisture the surface tension is established, and increased moisture has little effect on successful fracture formation.

4.1.3 Nozzle Design

The design of the nozzle had a significant effect on the ability to initiate fractures in the tank tests. The first nozzle used in the experiments was originally designed for clays and other fine grained soils for which pneumatic fracturing has been traditionally applied. The result of these sessions showed that air escaped along the injector and along the walls of the tank. Air escape had not been a problem in fine grained soils because of the tight seal formed around the injector owing to the cohesive nature of the soils. In the field, the air is sealed in by an inflatable packer in the well.

To overcome the air seal problem, several modifications were made to the basic nozzle. Initially, several flange-type seals were attached at various heights above the injector port. Fracture effectiveness improved, but the experimental results continued to be erratic. Finally, a 4 in. (10.2 cm) diameter double plate-type nozzle design (type G, Table 4.1) was determined to be most effective. The apparent advantage of this design was the ability to direct the air flow horizontally, and to focus it over a smaller area. The

double plate-type nozzle was utilized for the remainder of the experiments, and it is believed that the pneumatic "cutting" action provided by this design is crucial to fracturing a permeable formation, especially at low densities.

4.1.4 Wall Effects

The boundary conditions created by the test tank walls were also found to be significant in the bench scale study, and probably skewed the results compared with results of tests on the field scale. The vent pipes, which were placed in the tank corners to prevent excessive back pressure, clearly influenced the fracture patterns. There was a distinctive conical fracture shape in most tests, as the fractures inclined towards the vent wells. Another adverse wall effect was the existence of air voids around cobbles that were packed immediately adjacent to the tank wall. Injected air sometimes escaped through these voids, thereby preventing achievement of a successful fracture.

4.1.5 Refracture Behavior

Once a unsuccessful fracture injection occurred and the soil in the tank had been disturbed, it was generally not possible to refracture the tank. Also, if a successful fracture was purposely closed by decreasing the pressure, it was generally not possible to reopen the formation (exceptions: test nos. 21 and 38). This trend was especially apparent for the tank tests performed at lower moisture contents or lower dry densities, or both. It is suspected that the ability to reopen fractures will be enhanced after the graphite/glass frit mixture is injected. This aspect will be discussed further in Section

5.3. Overall, the results of the refracture tests suggest that during a field test it will be critical to achieve satisfactory fractures on the first attempt.

4.1.6 Aperture Control

Fracture aperture control is believed to be an important factor in the field application, although little attempt was made to control it during the bench scale studies. This is primarily because the first priority of these experiments was to achieve a fracture. Observed fracture apertures ranged from 1 to 6 in. (2.5 to 15.2 cm) throughout the testing. Provisions for improved aperture control will be incorporated into the field system. Additionally, the increased overburden is likely to reduce the fracture aperture.

4.1.7 Fracture Inclination

Another fracture characteristic observed in the bench scale tests was the tendency for the fracture to incline upwardly from the injection point. This is a significant finding, especially for larger injection radii in the field. During the bench scale tests the angle of fracture inclination ranged from 15° to 35°, with a predominant value in the range of 25° to 30°. The inclination angle within a single fracture was rarely constant, and it was usually steeper around the nozzle and flatter with increasing radius. The inclination angle may have been influenced by wall effects in the test tanks and the subsequent need for the vent wells. The tendency for fracture inclination at the field scale will have to be investigated.

4.1.8 Lens Formation

While excavating tanks following media injection, a significant difference was noted between the lens geometry of the sand and the graphite/glass frit. These tanks were carefully excavated to detail the shape of the dry media lens. Excavations were performed for one sand injection and two graphite/glass frit injections. Excavation of the sand injection in test no. 15 revealed that the lens was nearly continuous from the nozzle and throughout the plane of fracture. Displacement or "cutting" of the surrogate test soil was probably enhanced by sand injection, since the media is more dense and less viscous than the graphite/glass frit mixture.

The first tank excavated with a graphite/glass frit injection was from test no. 18.. In contrast to the sand injection, a continuous layer was observed at the fracture level, but the fracture level was 9 in. (23 cm) above the nozzle. The graphite/glass frit appeared to have traveled up along the injector pipe until it reached the fracture level. The lens was not traceable to the nozzle. This effect may be related to the difference in physical properties of the materials. The graphite/glass frit is less dense and also has self-lubricating properties, which may have allowed it to travel along the small annular space between the injector and the soil.

The second graphite/glass frit tank excavated after test no. 38 displayed a different behavior. For this test, the graphite/glass frit flow was started simultaneously with the initiation of the fracture. This created an initial heave followed by a visible fracture at the level of the nozzle which was instantly filled with the injected media. The lens measured 0.5 ft (15 cm) in thickness around the nozzle and 0.3 ft (9 cm) near the

tank walls. The average inclination of the lens was 24° from the nozzle to the tank wall. The explanation for this differing behavior is believed to be the beneficial effects of media caking in fracture propagation. There was also a significant amount of graphite/glass frit below the nozzle, which suggests that either the injection lifted the nozzle, or the injection followed a downward trajectory.

4.2 Conductivity Tests

4.2.1 Results

A total of four tank tests were performed with graphite/glass frit injection and the results are summarized in Table 4.2. The first conductivity test, test no. 18, resulted in an extremely conductive 2 in. (5.1 cm) lens. The average resistance measured across the electrodes was 0.80 ohms after fracturing, compared with 427 ohms before fracturing.

The objective of the second test, test no. 19, was to minimize the thickness of the graphite/glass frit lens. However, during the course of the injection, the air flow was prematurely reduced and part of the fracture collapsed. The collapse resulted in a discontinuous lens and no significant change in conductivity was measured.

In the third test, test no. 35, a relatively thin lens of graphite was successfully established with an average thickness of 0.5 in. (1.3 cm). However, the injection was terminated prematurely due to escape of the graphite/glass frit mixture around the injector resulting in no observable conductivity improvement. Another attempt was made to establish a connection between the electrodes and the injected media by driving a 2 in. (5.1 cm) casing around each electrode. The electrodes were then removed, the

soil within the casing extracted via vacuum, and the electrodes reinstalled and backfilled with the graphite/glass frit media. Upon removal of the casings, conductivity was checked again and no significant change was observed.

A fourth graphite/glass frit injection was performed for test no. 38. This experiment utilized two 0.5 in. (12.7 mm) diameter aluminum rods in lieu of the graphite electrodes. The smaller electrodes facilitated compaction of the soil in the tank, and improved experimental similitude. Another difference in this test, as previously discussed in Section 4.1.8, was the simultaneous introduction of graphite/glass frit flow at the point of fracture initiation. This injection produced a continuous graphite/glass frit lens averaging 5 in. (127 mm) thick. Measurements showed a conductivity increase of 21 times after injection of the graphite/glass frit (see Table 4.2).

An auxiliary test was performed to compare the conductive efficiency of the aluminum and graphite electrodes. A pair of electrodes of each material was placed in a tub filled with graphite/glass frit and the resistivity measured. The aluminum electrodes exhibited more than twice the resistance (21 ohms versus 10 ohms) of the graphite electrodes under the same test conditions. This partly explains why the conductivity improvement observed in test no. 38 was not as high as in test no. 18.

4.2.2 Discussion

The two successful graphite/glass frit injection tests (nos. 18 and 38) showed that a conductive link between two electrodes can be established below the soil surface using the pneumatic fracturing technology. The two unsuccessful tests were attributed to

Table 4.2 Graphite/Glass Frit Injection Conductivty Measurements

Fracture Session/ Tank No.	Pre-Injection			Post-Injection			Remarks
	Voltage (volts)	Current (mAmps)	Resistance (ohms)	Voltage (volts)	Current (mAmps)	Resistance (ohms)	
14/1	30	50	600	0.32	444	0.72	Average thickness of graphite/glass frit layer was 2 inches. Average resistance was 0.80 ohms.
	40	116	344	0.59	774	0.76	
	50	148	337	1.04	1,267	0.82	
	--	--	--	1.76	2,052	0.86	
	--	--	--	2.12	2,472	0.86	
14/2	30	50	600	30	59	508	Graphite/glass frit layer was non-continuous due to collapse of fracture resulting from lack of pressure control.
	40	116	344	40	78	513	
	50	148	337	50	82	610	
24/1	30	40	750	30	45	667	Graphite/glass frit layer averaged 0.5 in--Lack of conductivity is attributed to premature termination of injection.
	40	57	702	40	55	727	
	50	80	625	50	76	658	
24/1	--	--	--	30	60	500	Electrodes were removed, borehole reamed, electrode reinstalled and annulus backfilled with graphite, and conductivity remeasured. There was no significant difference, thus the lens is not continuous.
	--	--	--	40	90	444	
	--	--	--	50	110	455	
27/1	3	1	3000	1	11	91	Conductivity measured across aluminum electrodes.
	11	5	2200	16	132	121	
	50	20	2500	33	160	206	

operational difficulties leading to the formation of non-conductive lenses. Based on the results of tests using injection of air and air with silica sand or graphite/glass frit, it is believed that if a viable fracture can be established, the graphite/glass frit can be successfully injected. An important advantage of the graphite/glass frit as the dry injection media is its self-lubricating properties.

4.3 Horizontal Infiltrometer Tests

4.3.1 Results

The key experimental parameters and results for the eight horizontal infiltrometer test performed are presented in Table 4.3. The first test was performed using a volume of graphite (1501)/glass frit mixture that was approximately equal to the pore volume of the soil. No penetration was discernible and excessive caking at the face of the soil column was observed.

In the second test, the amount of graphite used for injection was decreased to one-fourth the pore volume, and a finer variety of graphite (No. 635) was used without the glass frit. Only 1 to 3 mm (0.04 to 0.12 in.) of interstitial penetration was attained as surface caking was predominant.

An even finer graphite (No. 205) was used in the third test. Again, interstitial penetration was limited to 1 to 3 mm (0.04 to 0.12 in.) and caking was observed on the surface. Additionally, 3 mm (0.12 in.) of penetration was observed along the interface between the soil and the mold.

Table 4.3 Summary of Infiltration Test Results

	CONDITIONS							PENETRATION		
Test No.	Soil Density (pcf)	Soil Moisture (wt %)	Injected Mixture	Source Pressure (psi)	Pressure Differential (psi)	Inital Flow (cfm)	Final Flow (cfm)	Over Face (mm)	At Boundary (mm)	Remarks
1	100	5	Graphite (1501) & glass frit	60	4	8.5	4.5	0	0	Excessive caking
2	103	6	Graphite (635)	60	4	8.5	3.5	1-3	0	--
3	105	6.5	Graphite (205)	60	4	8.5	7.5	1-3	3	--
4	99	5	Glass frit	60	4	8	7	1-2	2	--
5	100	3.1	Graphite (205)	60	4	9	7	1-2	2-3	--
6	98	2.1	Graphite (205)	2,400	37	>9	>9	1-3	4	--
7	100	3	Graphite (205)	2,400	37	>9	>9	1-3	1-3	--
8	114	3	Graphite (205)	2,400	37	>9	>9	1-2	4-5	--

The fourth test utilized just glass frit as the injection media. Penetrations of 1 to 2 mm (0.04 to 0.08 in.) was attained into the soil face and along the soil-mold boundary. The glass frit may have penetrated farther into the soil, but its light color made the exact penetration distance difficult to discern.

Since penetration along the boundary between the mold and the soil was observed in the third and fourth tests, a cobble was placed at the inlet end of the mold in test five to examine potential media transport along the soil-cobble boundary. Graphite No. 205 was the injection media for this test. Results revealed 1 to 2 mm (0.04 to 0.08 in.) of surface penetration, 2 to 3 mm (0.08 to 0.12 in.) of penetration along the soil-mold boundary and 2 to 3 mm (0.08 to 0.12 in.) of penetration at the soil-cobble interface.

Since the infiltrometer tests to this point were conducted at a relatively low pressure differential of 4 psi (27 kPa), the pressure differential was increased to 35 psi (241 kPa) for the remainder of the tests to investigate the effect of pressure on interstitial penetration. Additionally, the moisture content was reduced from 5 to 6 wt% to 2 to 3 wt% to more closely simulate field conditions.

The sixth test utilized graphite No. 205 as the injection media. Scouring of the soil at the inlet ranged from 1 to 5 mm (0.04 to 0.20 in.) because of the higher pressure. Despite significant scouring, the graphite only penetrated 1 to 3 mm (0.04 to 0.12 in.) through the soil and 4 mm along the soil-mold boundary.

Graphite No. 205 was used as the injection media in the seventh test. Again, scouring of the soil was observed at the inlet and media penetration was estimated to be 1 to 3 mm (0.04 to 0.12 in.) along the soil-cobble and soil-mold boundaries.

To more closely simulate field soil conditions, the last test was performed with a soil mixture consisting of 50% soil passing sieve No. 8 and 50% gravel (1.0 to 2.5 cm (0.4 to 1.0 in.) in diameter). Graphite No. 205 was used as the injection media. Soil scouring occurred at the inlet end and graphite penetration of 1 to 2 mm (0.04 to 0.08 in.) through the soil interstices was attained. A penetration of 4 to 5 mm (0.16 to 0.20 in.) was observed along the soil-mold boundary.

4.3.2 Discussion

The infiltrometer tests showed that interstitial penetration will not be a significant mechanism in starter path creation, even when using a very fine graphite or glass frit. No significant penetration was observed in the initial experiments using a coarser variety of graphite and low pressure gradients. When a finer variety of graphite and higher pressure gradients were used, penetration improved but still remained minimal. Maximum penetration was observed along the soil-cobble and soil-mold interfaces, but still did not exceed 5 mm (0.2 in.). In each experiment, a drop in the flow rate occurred after each slug of the dry media was injected. The drop in the flow rate was attributed to surface caking, as the dry media clogs the soil interstices.

While the results of the infiltrometer tests were generally negative from a transport perspective, they do have important implications for fracture propagation. These implications will be discussed in Section 5.3.

4.4 Segregation Tests

4.4.1 Results

Two different tests were performed to examine whether the two components of the starter path will separate during the injection process. Such separation would have an adverse effect on the melt. Both tests exhibited similar results. No uniform patterns of segregation were observed, although zonal segregation was apparent at some locations in the tube. At the entrance end of the tube, adjacent to the point of injection, turbulence prevented significant deposition of media. In the central region of the tube, the flow was more laminar which allowed for significant deposition of the graphite/glass frit mixture. Some vertical segregation was visible along the central region, as the graphite concentration was higher towards the upper free surface. Horizontal segregation was observed at the end of the tube farthest from the injection point, as the deposited media consisted mostly of graphite at this location. The horizontal segregation was attributed to the loss of glass frit through the end filter.

4.4.2 Discussion

The results of the bench scale segregation tests indicate that there is some potential for segregation of the graphite and glass frit components. The potential for vertical segregation is believed to be greater than horizontal segregation. Despite the observed segregation, the components are judged to be sufficiently mixed for initiating the ISV melt. Further bench scale and model studies on segregation phenomena should be

performed as the integrated PF/ISV technology develops. If necessary, the particle size

and/or mixture proportions could be adjusted to minimize segregation.

CHAPTER 5

MODEL ANALYSIS OF MEDIA TRANSPORT

This chapter presents a model analysis of dry media transport in pneumatically induced fractures. Satisfactory transport and filling of the fracture planes with starter path media is essential to a successful melt initiation with the ISV process. Ideally, the fracture should extend farther than the radii of the electrodes. Also, the fracture must be continuous to support an uninterrupted starter path lens. This chapter will present the background, development and results of the model analyses that describe these physical processes.

The first model analysis predicts fracture dimensions by estimating pressure and velocity distributions within the formation (Section 5.1). The second model analysis estimates the critical fluid velocity necessary to keep the injected media in suspension during transport (Section 5.2). The third model analysis examines the potential for transport of injected media directly through the interstitial pore space of the formation soil (Section 5.3).

5.1 Fracture Dimensions

In order to estimate fracture dimensions, it is necessary to determine the pressure and velocity distributions within the fracture. Pressure and velocity affect the distance the fracture propagates, as well as the ability of the injected air stream to carry the injected

media into the fracture. This section details the background, development, and results of these parameters.

5.1.1 Estimation of Pressure Distributions

5.1.1.1 Background and Development

Pressure is the parameter which controls fracture initiation in a formation. Injection pressure also supports the weight of the soil overburden as the fracture propagates away from the borehole.

Pressure distributions within a fracture during injection were predicted with Equation 5.1, which was based on the cubic law for radial flow of compressible fluids (Nautiyal, 1994). The equation also accounts for gas compressibility effects and is based on the assumption that the conditions are isothermal.

$$Q = -\frac{\pi g b^3 (P_1^2 - P_2^2)}{12 v P_1 \ln(R_2/R_1)} \qquad (5.1)$$

where:

Q = volumetric flowrate (L^3/T)

b = fracture aperture (L)

v = kinematic viscosity (L^2/T)

g = acceleration due to gravity (L/T^2)

P_1, P_2 = pressures at R_1 and R_2, respectively, in height of fluid (L)

R_1, R_2 = radial distance from extraction well ($R_1 < R_2$) (L)

Assuming that injection pressure, P_1, and flow, Q, are known, the equation can be solved

for fracture pressure, P_2, at a particular radius, R_2, using Equation 5.2.

$$P_2 = \frac{\sqrt{P_1^2 - \frac{12 P_1 Q v \cdot \ln(R_2/R_1)}{\pi g b^3}} - 8056.352}{548.05} \tag{5.2}$$

The constants in the equation, 8056.352 and 548.05, are the conversions of 14.7 psi and 1

psi, respectively, to absolute meters of air. The resulting P_2 is measured in absolute

meters of air and the radius, R_2, is measured in meters.

Since this equation is a derivation of the cubic law for fluid flow in fractures, the

value chosen for the exponent of the fracture aperture, b, is an important decision. For

purely laminar flow, the exponent is equal to three, which maximizes flow and minimizes

pressure in the fracture. Therefore, the laminar case is the most conservative case in

terms of pressure distribution, and thus the most conservative case for predicting the

fracture radius. The pressure distribution calculation does not consider leakoff of air into

the formation, which is discussed in Section 5.1.2.

5.1.1.2 Results

The pressure distribution model, solved for typical field parameters set at a 2 in. (5 cm)

aperture and 3,000 cfm (1.42 m^3/s) injection flow rate, is presented in Appendix A. The

analysis also required an assumption of injection pressure, P_1, which was estimated to be

40 psi (276 kPa) based on a study of fracture maintenance pressure (King, 1993).

The results using these input assumptions are summarized in Appendix A. As indicated, the pressure drop along the fracture is minimal. This pressure behavior results from the relatively large 2 in. (5 cm) aperture assumed for the calculation, which is the aperture expected in the field condition.

5.1.2 Velocity Distribution

5.1.2.1 Background and Development

The importance of predicting air velocity in the fracture is two-fold. The velocity determines both the radius of fracture propagation and the ability to transport the graphite/glass frit media through the fracture. This section addresses velocity determination for fracture propagation. Transport of graphite/glass frit media is discussed in the next section.

The assumed physical model for velocity distribution is shown in Figure 5.1. The velocity in the fracture at a particular radius is calculated by dividing the volumetric flow at that point by the area of the fracture. As the radius of fracture increases, flow volume is continuously lost into the formation by "leakoff". Flow losses due to leakoff are calculated using Darcy's law and established gradients by analyzing successive annular rings. Using a finite difference approach, this may be expressed as:

$$Q_R = K_p \cdot (i_{pu} + i_{pd}) \cdot \pi \cdot [(R+0.5)^2 - (R-0.5)^2] \tag{5.3}$$

where:

Q_R = volumetric flow due to leakoff at radius R (L^3/T)

K_p = pneumatic conductivity (L/T)
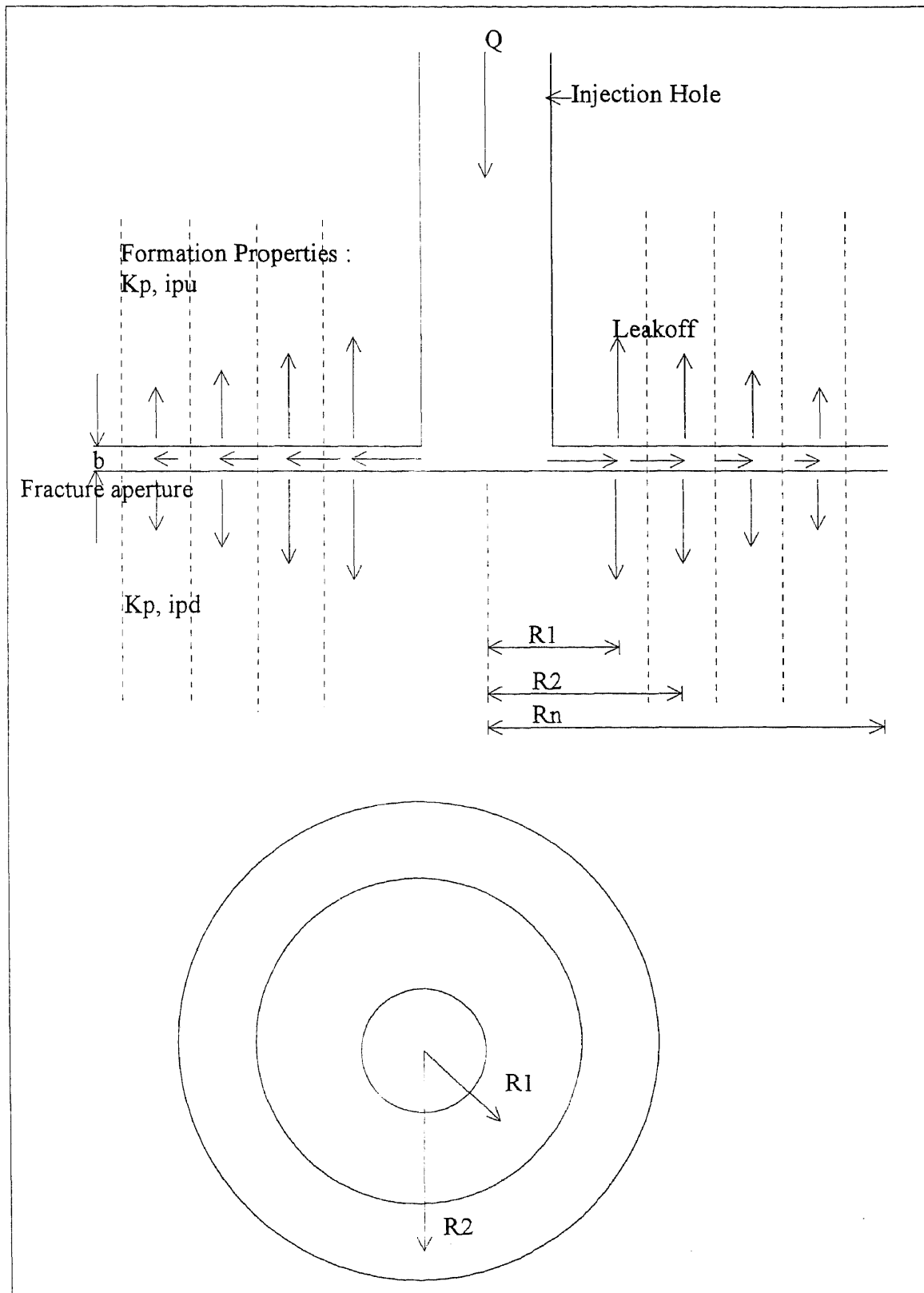
Figure 5.1 Physical Model for Velocity Distribution

$i_{p\,u}$= pneumatic gradient (up), dimensionless

$i_{p\,d}$= pneumatic gradient (down), dimensionless

R = radius from injection point in fracture (L)

The equation accounts for the leakoff into both the upper and lower boundaries of the fracture according to the pneumatic gradient through the adjacent porous media. Due to the proximity of the ground surface, the upward gradient will be larger than the downward gradient. The exact ratio will depend on the depth of injection and the formation stratigraphy.

The air velocity in the fracture will decrease with increasing radius from the injection point due to leakoff. The velocity at any radius, R, may be determined using Equation 5.4:

$$V_R = \frac{Q - \sum_{R=1}^{R} Q_R}{2\pi Rb} \tag{5.4}$$

where:

V_R=velocity in the fracture at radius, R (L/T)

Q=volumetric flow into the fracture (L^3/T)

b=fracture aperture (L)

Equation 5.4 represents the total volumetric flow in the fracture divided by the cross-sectional area of the fracture.

This model does not consider increases in effective radius which may result from the cutting action expected with the plate-type nozzle proposed for use. The model also

neglects the effects of the injected dry media which may reduce pneumatic gradients due to surface caking on the fracture surfaces.

5.1.2.2 Results

The velocity distribution model was solved for a range of assumed values for aperture (b), pneumatic conductivity (K_p), and pneumatic gradient (i_{pu} and i_{pd}). This approach allowed the sensitivity of the model to be checked, since the field parameters are not exactly known. The calculations are contained in Appendix B, and the model solutions and the corresponding assumptions are summarized in Table 5.1.

Table 5.1 Maximum Radial Distance Estimations

K_p^* (m/s)	i_{pu}^{**}	i_{pd}^{**}	b (m)	Max. Radial Distance (m)
0.0007	4500	1500	0.05	0
0.0007	1500	500	0.05	0
0.00007	2250	750	0.025	1.1
0.000007	1500	500	0.05	5.3
0.000007	4500	1500	0.05	2.9

* The hydraulic conductivity of the Hanford Formation is reported to range from 0.001 to 0.01 m/s. Converting to pneumatic conductivity, and extending the lower boundary of K_p one order of magnitude to account for caking effects, a range of 0.000007 to 0.0007 m/s was used for analysis.

** The upward pneumatic gradient for leakoff was estimated at a depth of 5 m. Due to the absence of an atmospheric boundary, the downward gradient was assumed to be one third of the upward gradient.

The results of the velocity distribution model indicate that flow dissipates rapidly in the formation, although it appears that effective radii up to a few meters are attainable.

The analysis also suggests minimal fracture propagation for the combination of high formation permeability and gradient. Such behavior may be expected if fracture propagation is attempted in very coarse, highly permeable soil. In summary, the results show that injection flow rate is the primary parameter which controls fracture propagation and radius.

5.2 Media Transport in Fractures

The transport of media in the fracture network is another essential part of integrating pneumatic fracturing with in situ vitrification. The fluid velocity needed to keep the graphite/glass frit particles in suspension is central to determining the dry media distribution.

Two transport models, the Shields diagram and the dust transport methods, were used to investigate the critical fluid velocity needed to counteract the settling velocity for each dry media component. Three different methods to calculate settling velocity were used in the dust transport method. The first method was the traditional Stokes Law method, which assumes the particles to be spherical. The other two methods, the Chien and Ganguly methods, account for nonspherical particle shape.

5.2.1 Shields Diagram

The Shields diagram method (Pettijohn et al., 1973) was used to investigate the transport of the starter path media in the laminar flow case. This method has been adapted to the

double boundary case of the pneumatic fracture from the single boundary application by Boggs (1987) using a stream bed, or bed exposed to a wind event.

5.2.1.1 Background

The Shields diagram correlates dimensionless shear stress with the Reynolds grain number, and is shown in Figure 5.2. It is widely used by sedimentologists to determine if particles will settle or be entrained by the fluid. It is a flexible method which can be used for wind transport, as well as a variety of water transport conditions. Points above the curve indicate that grains on the bed are entrained by the fluid and are in motion, while points below the curve indicate that the grains in the fluid are settling, and also that grains on the bed are not being entrained. Entrainment is the process of lifting resting grains from the bed or otherwise putting them in motion. The entrainment velocity is studied since the forces needed to entrain a particle are normally greater than the forces to keep a particle in suspension and transport it. Therefore, the critical velocity necessary to counteract particle settling will be defined in the remainder of this study as the entrainment velocity.

At lower Reynolds grain numbers, which is in the extrapolated region of the Shields diagram, the value of the dimensionless shear stress increases steadily to values greater than 0.1. The trend of the Shields diagram in this region is due to the presence of the formation of a viscous sublayer at the lower Reynolds grain numbers, which is chiefly a result of the small particle diameter. The small particles create a smooth boundary for the fluid to flow and therefore all particles lie within the viscous sublayer,
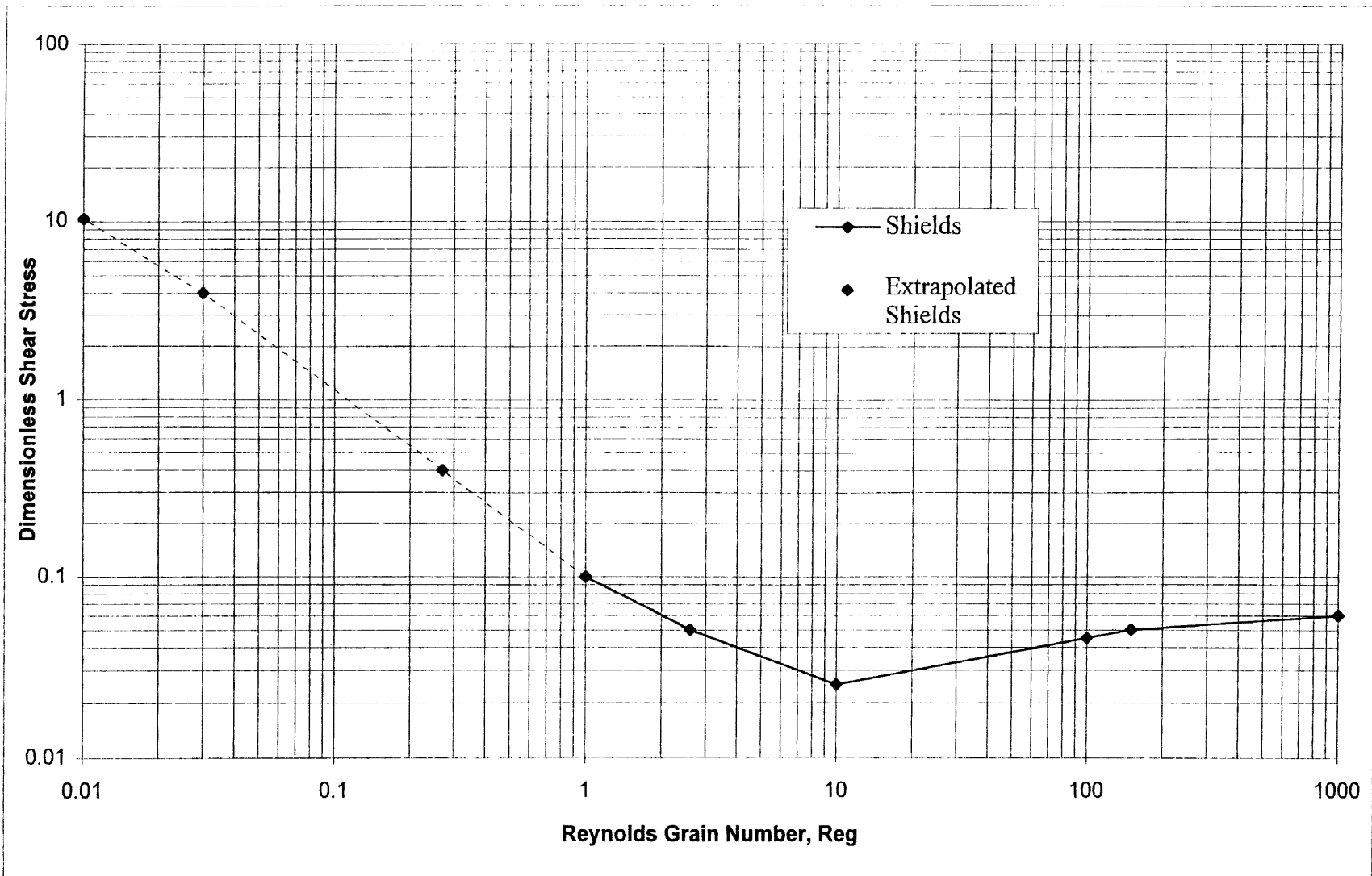
Figure 5.2 Shields Diagram (Modified from Boggs, 1987)

where flow is essentially nonturbulent and instantaneous velocity variations are less than in the lowermost part of the overlying turbulent boundary layer (Boggs, 1987). Note that the extrapolated data curve in Figure 5.2 in the range of Reynolds grain numbers 1 to 0.1 is included in the original diagram. For the purposes of the present analysis, the extrapolated curve was extended for Reynolds grain numbers in the range of 0.1 to 0.001 using the same slope.

5.2.1.2 Development

The Shields diagram is plotted using two dimensionless parameters, dimensionless shear stress and the grain Reynolds number. The dimensionless shear stress, τ^*, is defined as:

$$\tau^* = \frac{\tau_0}{(\gamma_s - \gamma_f)d} \qquad (5.5)$$

where:

τ_0 = boundary shear stress (L/T)

γ_s = specific gravity of the particles (M/L^3)

γ_f = specific weight of the fluid (M/L^3)

d = particle diameter (L)

Thus, the value of the dimensionless shear stress increases with boundary shear stress. The boundary shear stress is the product of the dynamic viscosity, μ, and the velocity profile, dV/dy.

The Reynolds grain number, R_{eg}, is the other parameter used in the diagram. The Reynolds grain number differs from the traditional Reynolds number, R_e, slightly. By

substituting the particle size, d, and friction velocity, U^* (L/T), for length and flow velocity in R_e, the grain Reynolds number becomes:

$$R_{eg} = \frac{U^* d}{\nu} \qquad (5.6)$$

where ν is the kinematic viscosity (L^2/T). The friction velocity is a measure of turbulent eddying, which is more appropriate than flow velocity because turbulence has a greater effect on the entrainment of particles. The friction velocity term in Equation 5.6 is then evaluated to calculate the Reynolds grain number. The friction velocity is defined as:

$$U^* = \sqrt{\frac{\tau_0}{\rho}} \qquad (5.7)$$

where ρ is the density of air (M/L^3). After separating dV and dy and evaluating, the resulting expression for the Reynolds grain number is:

$$R_{eg} = \frac{\sqrt{\frac{2\mu \cdot V}{b \cdot \rho}} \cdot d}{\nu} \qquad (5.8)$$

Note that Equation 5.8 is the expression for the Reynolds grain number under laminar flow conditions.

The entrainment velocity for laminar conditions, V, can be determined by solving for V in the boundary shear stress term, τ_0. The result is shown in Equation 5.9.

$$V = \frac{R_{eg}^2 \cdot \nu \cdot b}{2d^2} \qquad (5.9)$$

The entrainment velocity under all flow conditions is at the intersection of each parameter line and the Shields diagram. The equations for turbulent flow are derived in Appendix C.

There are several complicating factors which the Shields diagram does not consider when determining the critical threshold for grain movement. One of these factors, local eddies, create instantaneous fluctuations in boundary shear stress that stimulate local grain movement. The cohesive nature of clays and silts is also not considered in the Shields diagram method. Soil cohesion results in little to no grain movement at or above the critical threshold. Additionally, the contact of wind entrained particles with particles at the bed can initiate grain movement below the entrainment velocity.

5.2.1.3 Results

Calculated values of the Reynolds grain number are shown in Table 5.2 for the d_{10} and d_{50} of both the graphite and the glass frit particles. These values were calculated by substituting the appropriate specific gravities and a range of velocities into Equations 5.5 and 5.8 that cause each parameter line to intersect the Shields diagram.

Table 5.2 displays the calculated entrainment velocities for each particle. Figure 5.3 graphically presents the Reynolds grain number and dimensionless shear stress for each particle parameter over the selected velocity ranges.

Table 5.2 Entrainment Velocities for Laminar Conditions-Shields Diagram Method

Particle diameter (m)		Reynolds grain number	Entrainment velocity (m/s)
$d_{gr}10$	0.0002	0.19	0.34
$d_{gr}50$	0.0004	0.39	0.36
$d_{gf}10$	0.00002	0.019	0.34
$d_{gf}50$	0.000043	0.033	0.22
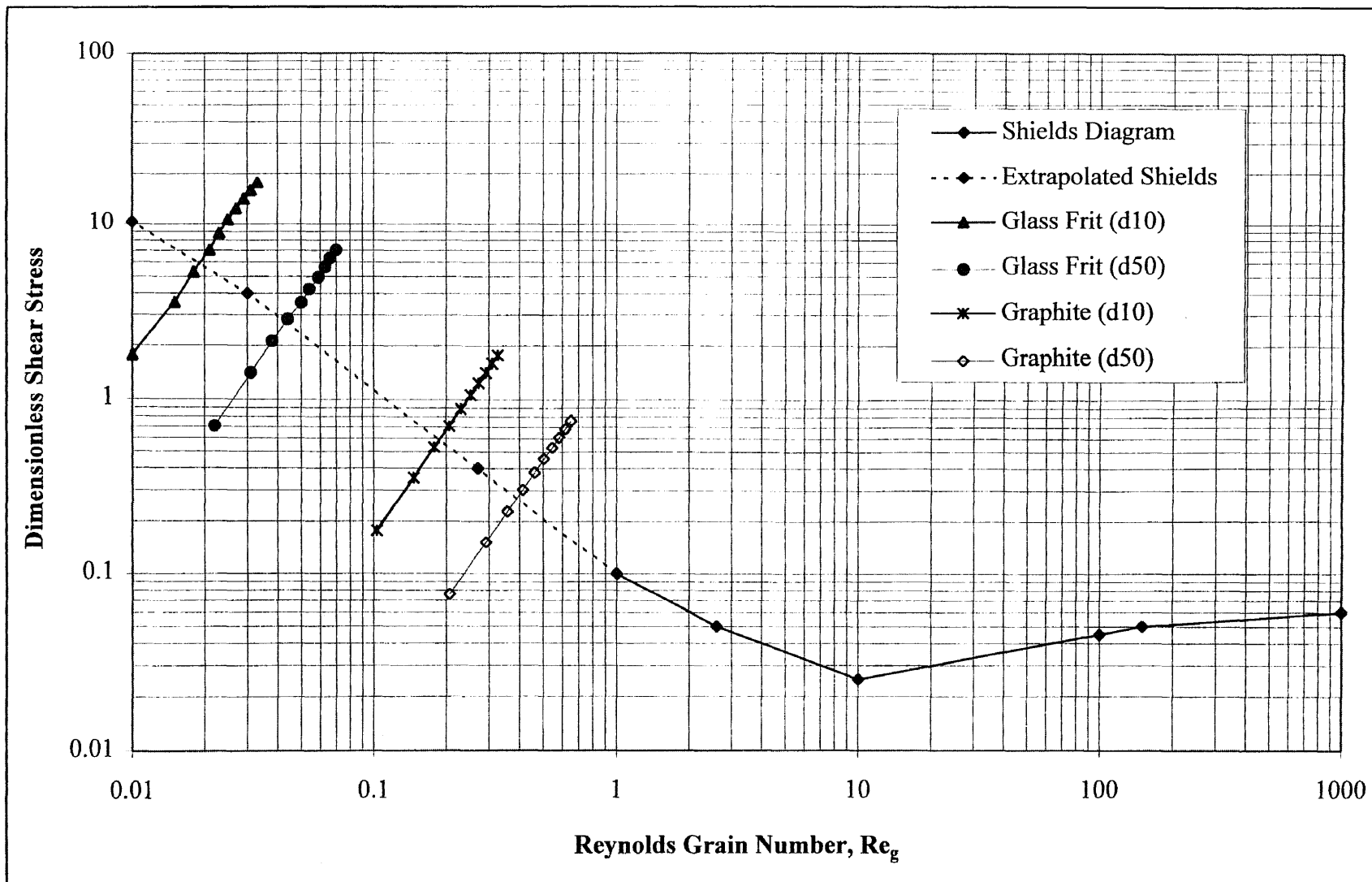
Figure 5.3 Shields Diagram Method (Laminar Flow)

Supporting calculations for the laminar and turbulent cases are presented in Appendix C. The turbulent case results are not presented in this section due to the uncertainty in determining the coefficient of turbulent exchange, as the entrainment velocities in the turbulent case were generally three orders of magnitude lower than the laminar condition.

5.2.2 Dust Transport

The dust transport method was used to investigate dry media transport in a fracture for turbulent flow. To calculate the entrainment velocity by the dust transport method, the settling velocity had to be determined. Three different methods were used to calculate settling velocity. Stokes law was used for spherical particles, and the Chien and Ganguly methods were used to account for the plate-like shape of the graphite particles.

5.2.2.1 Background

The dust transport approach was developed by Tsoar and Pye (1987) in their investigation of desert loess formations. The primary application of this method is to small particles, 1 to 50 micrometers, since they are likely to be transported long distances. The key parameters for determining the time and distance that the dust particles are transported are the settling velocity of the particle, U_f, and fluid velocity and turbulence.

Tsoar and Pye state that the entrainment velocities for particles finer than 50 μm vary with the grain size, but are normally in the range of 20 to 60 cm/s (8 to 24 in./sec).

The entrainment velocity for the glass frit is expected in this range, but the entrainment velocity of the graphite is not because of larger grain size. The dust transport method suggests that particle settling velocities be calculated using Stokes Law. Two other methods for calculating settling velocity will also be used to account for the large, more irregular shape of the graphite particles.

5.2.2.2 Development

The velocity and turbulence of the flow are considered in one term, the friction velocity, which is defined as:

$$U^{*2} = (v + \varepsilon)\frac{dV}{dz} \tag{5.10}$$

where:

U^* = friction velocity (L/T)

v = kinematic viscosity (L^2/T)

ε = coefficient of turbulent exchange (L^2/T)

dV/dz = rate of shearing strain (T^{-1})

Separating, integrating, and substituting the settling velocity for the friction velocity in Equation 5.10 results in the following:

$$V = \frac{U_f^2 \cdot b}{2(v + \varepsilon)} \tag{5.11}$$

By analyzing the wind velocity two dimensionally, Tsoar and Pye set 'u' as the velocity in the direction of the flow and 'w' as the velocity perpendicular to the direction of the flow. The vertical fluctuating velocity, w', was defined as the difference of the

vertical velocity, 'w', and the mean vertical velocity, $\overline{w}$. Thus, the standard deviation of

w', $\sigma = \sqrt{\overline{w'^2}}$ represents the force opposing the tendency of small particles to settle.

Tsoar and Pye determined that a particle should remain in suspension if $\sqrt{\overline{w'^2}} > U_f$.

The two main modes of transport are suspension and saltation. Pure suspension

occurs when the settling velocity is very small relative to the friction velocity. The upper

limit of pure suspension is $U_f/U^* \approx 0.7$. Pure saltation occurs when vertical turbulent

components have no significant effect on the particle trajectories. The process of

transport between these two modes is termed "modified saltation", where both the settling

velocity and inertia have influence on the particle trajectory.

The coefficient of turbulent exchange, ε, from Equation 5.10 was derived using

the following equation:

$$\varepsilon = \sqrt{\overline{w'^2}}\, l \qquad (5.12)$$

where l is the mixing length, defined as the characteristic length perpendicular to the

main flow covered by the mixing of air particles in the turbulent flow before their

momentum is absorbed. Tsoar and Pye (1987) used an earlier equation for mixing length,

$l=\alpha kz$, where $\alpha=1$ for neutral atmospheres, k is the von Karman constant = 0.4, and z, the

height above the boundary layer. Using $\varepsilon = \alpha \sqrt{\overline{w'^2}}\, kz$ as the expression for coefficient of

turbulent exchange and substituting $\sqrt{\overline{w'^2}} = U_f$ for the critical case, the following is

obtained:

$$\varepsilon = 0.4 \cdot U_f z \qquad (5.13)$$

Equation 5.13 was used as the expression for the coefficient of turbulent exchange in the determination of entrainment velocities. To evaluate this equation, settling velocities were calculated using the three methods discussed later in this section.

Entrainment velocities can also be calculated under laminar conditions, although only the turbulent results of dust transport are presented in the following sections due to the uncertainties in the laminar results. However, the laminar results are contained in Appendix C.

5.2.2.3 Results using Stokes Law

Stokes law defines the settling velocity of a particle by:

$$U_f = \frac{\rho_s g d^2}{18\mu}$$
(5.14)

where:

U_f = settling velocity (L/T)

ρ_s = density of solid media (M/L^3)

g = acceleration due to gravity (L/T^2)

d = particle diameter (L)

μ = dynamic viscosity (M/L-T)

Equations 5.13 and 5.14 were used to calculate the coefficient of turbulent exchange and the settling velocity, respectively. The results using Stokes Law are presented in Table 5.3.

Table 5.3 Summary of Settling Velocity and Coefficient of Turbulent Exchange

Size Parameter	Particle size (m)		Settling Velocity, U_t (m/s)		Coeff. of Turb. Ex., ϵ (m^2/s)	
	Graphite	Glass frit	Graphite	Glass frit	Graphite	Glass frit
d_{10}	0.0002	0.00002	2.47	0.03	0.025	0.0003
d_{50}	0.0004	0.000043	9.88	0.13	0.099	0.0013
2/3 d_{10}	0.000134	------	1.11	------	0.011	------
2/3 d_{50}	0.000268	------	4.4	------	0.044	------

The values for settling velocity and coefficient of turbulent exchange for the graphite were also calculated for d_{10} and d_{50} parameters reduced by one-third in an attempt to account for the plate-like shape of the graphite particles.

Entrainment velocities were then calculated using the results from Table 5.3 and Equation 5.15, and are presented in Table 5.4.

Table 5.4 Entrainment Velocities for Turbulent Conditions-Stokes Law Method

Size parameter	$V_{graphite}$ (m/s)	$V_{glass frit}$ (m/s)
d10	6.1	0.05
d50	24.6	0.29
2/3 d10	2.8	------------
2/3 d50	11.0	------------

using $v = 1.5 \times 10^{-5}$ m^2/s.

Additional details of these calculations of this method are presented in Appendix C.

5.2.2.4 Results using Chien Method

The second approach used to calculate particle settling velocities was based on a method by Chien (1993). He developed a new correlation to predict the settling velocity of irregularly shaped particles in Newtonian and non-Newtonian fluids for all slip regimes. Since pneumatic fracturing predominantly uses air, only the Newtonian case was investigated. Chien developed a relationship between the drag coefficient and the Reynolds grain number using experimental data.

Chien investigated three slip regimes: laminar, transitional and turbulent. The laminar slip regime was found in the settling of smaller particles (<0.007 in.(0.17 mm)) in which the settling velocity increased proportionally to the square of the grain size. The turbulent slip regime occurred during the settling of larger particles (>0.05 in.(1.3 mm)). The settling velocity in this regime increased proportionally to the square root of the grain size. A transitional regime was identified for grain sizes between the laminar and turbulent regimes.

In the laminar slip regime, the settling velocity is chiefly affected by the viscosity and density of the fluid. However, the settling velocity in the turbulent slip regime is affected mostly by the density of the fluid and the surface characteristics of the particle (Chien, 1993). Chien stated that for most fluids a Reynolds grain number less than 10 indicates laminar slip, while a value greater than 50 suggests a turbulent slip regime.

Chien compiled experimental data from several different studies for irregularly shaped particles in different fluids and slip regimes. The data were manipulated to obtain

a plot of drag force versus Reynolds grain number. Equation 5.15 defines the relationship between the two parameters for shape factors between 0.2 and 1.0.

$$C_d = \frac{30.0}{R_{eg}} + \frac{67.289}{e^{5.030\phi_s}} \tag{5.15}$$

where:

C_d = drag coefficient, dimensionless

R_{eg} = Reynolds grain number, dimensionless

ϕ_s = shape factor, dimensionless

By combining traditional definitions of the drag coefficient and the Reynolds grain number with the correlation obtained from the experimental data, Chien rearranged Equation 5.15 and solved for the positive root of the settling velocity term, which is expressed as:

$$U_f = 0.0002403 e^{5.030\phi_s} \left(\frac{\mu}{d \cdot \rho_f} \right) \left[\sqrt{1 + 920790.49 e^{-5.030\phi_s} \cdot d \left(\frac{\rho_s}{\rho_f} - 1 \right) \left(\frac{d \cdot \rho_f}{\mu} \right)^2} - 1 \right] \tag{5.16}$$

where:

U_f = settling velocity (L/T)

μ = dynamic viscosity (M/L-T)

d = particle diameter (L)

ρ_f = fluid density (M/L^3)

ρ_s = particle density (M/L^3)

Equation 5.16 was solved using graphite particle shape factors of 0.3 and 0.45 for both

the d_{50} and d_{10} sizes and 1.0 for the glass frit particles. The settling velocity results using

this method are shown in Table 5.5.

Table 5.5 Summary of Settling Velocity Calculations-Chien Method

Particle/Parameter	Shape Factor	Diameter		Settling Velocity, U_t	
		in.	m	ft/sec	m/s
Graphite/d_{50}	0.3	0.016	0.0004	2.44	0.74
Graphite/d_{50}	0.45	0.016	0.0004	3.48	1.06
Graphite/d_{10}	0.3	0.008	0.0002	1.58	0.48
Graphite/d_{10}	0.45	0.008	0.0002	2.17	0.8
Glass Frit/d_{50}	1	0.0017	0.000043	0.35	0.11
Glass Frit/d_{10}	1	0.00079	0.00002	0.08	0.02

Additional supporting calculations, including the approach for determining the

shape factors, are described in Appendix C.

Using Equation 5.13, these settling velocities were then used to calculate the

coefficients of turbulence. Finally, Equation 5.11 was used to calculate the entrainment

velocities shown in Table 5.6.

Table 5.6 Entrainment Velocities for Turbulent Conditions-Chien Method

Particle/Parameter	Shape Factor	Coefficient of Turb. Ex., ε (m^2/s)	Entrainment Velocity, V (m/s)
Graphite/d_{50}	0.3	0.0148	0.92
Graphite/d_{50}	0.45	0.0212	1.32
Graphite/d_{10}	0.3	0.0096	0.60
Graphite/d_{10}	0.45	0.016	1.0
Glass Frit/d_{50}	1	0.0022	0.14
Glass Frit/d_{10}	1	0.0004	0.02

5.2.2.5 Results using Ganguly Method

The third approach to calculate particle settling velocities was based on a method developed by Ganguly (1990), which determines the settling velocity of solids in a fluidizing column of water. The Ganguly method determined particle settling velocities experimentally using close-cut size fractions of coal, graphite and sand, as well as other solids. Experimental values for the Reynolds grain number at the settling velocity were empirically correlated with the particle shape factor and the Archimedes number, which considers grain size, densities of the liquid and the solid, and liquid viscosity. The Archimedes number is defined as:

$$Ar = \frac{d^3 \cdot g \cdot \rho_f \left(\rho_s - \rho_f \right)}{\mu^2} \tag{5.17}$$

where:

Ar = Archimedes number, dimensionless

The empirical correlation for Reynolds grain number presented by Ganguly is:

$$R_{eg} = 0.103 \cdot Ar^{0.804} \cdot \phi_s^{0.745} \tag{5.18}$$

where:

ϕ_s = shape factor, dimensionless

Note that the Ganguly method is valid for Archimedes numbers between 53 and 3,761 and shape factors between 0.5 and 0.974.

To calculate particle settling velocities using the Ganguly method, the Archimedes number was first determined for each particle parameter using Equation 5.17. The Archimedes number was then substituted into Equation 5.18 with the shape factors used in the Chien method. The resulting Reynolds grain number was equated to the traditional equation for the Reynolds grain number and solved for the settling velocity. The resulting settling velocity is:

$$U_f = \frac{R_{eg} \cdot \mu}{d \cdot \rho_f} \qquad (5.19)$$

Results using this equation are shown in Table 5.7 and detailed calculations are contained in Appendix C.

Table 5.7 Summary of Settling Velocity Calculations-Ganguly Method

Particle/Parameter	Shape Factor	Settling Velocity, U_f (m/s)
Graphite/d_{50}	0.3	1.42
Graphite/d_{50}	0.45	1.92
Graphite/d_{10}	0.3	0.53
Graphite/d_{10}	0.45	0.72
Glass Frit/d_{50}	1	0.17
Glass Frit/d_{10}	1	0.06

Entrainment velocities for the Ganguly method settling velocities were calculated using the dust transport method. These results are presented in Table 5.8.

Table 5.8 Entrainment Velocities for Turbulent Conditions-Ganguly Method

Particle/Parameter	Shape Factor	Coefficient of Turb. Ex., e (m^2/s)	Entrainment Velocity, V (m/s)
Graphite/d_{50}	0.3	0.028	1.8
Graphite/d_{50}	0.45	0.038	2.4
Graphite/d_{10}	0.3	0.011	0.66
Graphite/d_{10}	0.45	0.014	0.9
Glass Frit/d_{50}	1	0.003	0.21
Glass Frit/d_{10}	1	0.001	0.07

Although the shape factors for the above results are not in the recommended range for the Ganguly equation, the values are nevertheless considered reasonable.

5.2.3 Summary of Fracture Transport

Two methods, the Shields diagram method and the dust transport method, were used to examine dry media transport in fractures and to evaluate the potential for segregation of starter path material. The entrainment velocities or critical fluid velocities under laminar conditions were estimated using the Shields diagram method, while the dust transport method was used for turbulent conditions. Stokes Law, the Chien method and the Ganguly method were used to calculate the particle settling velocities, on which the dust transport method is based. The settling velocities for graphite and glass frit using the various methods are shown in Figure 5.4 and 5.5, respectively.

The average entrainment velocities under laminar conditions were estimated to be 0.35 m/s (1.15 ft/sec) for graphite and 0.28m/s (0.92 ft/sec) for glass frit. For turbulent conditions, the average entrainment velocity for graphite particles using the Chien and Ganguly estimates of settling velocity was 1.2 m/s (3.94 ft/sec). The average

entrainment velocity for the glass frit, using all three of the settling velocity methods, was 0.14 m/s (5.51 ft/sec).

Entrainment velocities in a turbulent regime would be expected to be less than those in a laminar regime, because turbulent eddies allow for entrainment at lower velocities. As expected, the turbulent results are less than laminar results for the glass frit. However, the turbulent results are greater than the laminar results for graphite, which was not expected. This discrepancy was attributed to the inability to accurately estimate the coefficient of turbulent exchange, and the uncertainty of the atmospheric stability coefficient. In addition, this method was derived for dust size particles and may not accurately represent the transport of particles as large as the graphite flakes.

The results of Shields diagram method are believed to be more reliable than the dust transport results, as the Shields method requires fewer crucial assumptions. The results of both methods suggest that segregation will not be significant, as the entrainment velocities are much less than air velocities in the fracture determined in Section 5.1. Therefore, it is likely that the particles will be packed into the lens before segregation of the particles will occur. Note that although the potential for segregation increases with radius, higher flow rates and thus higher velocities will tend to counteract this tendency.
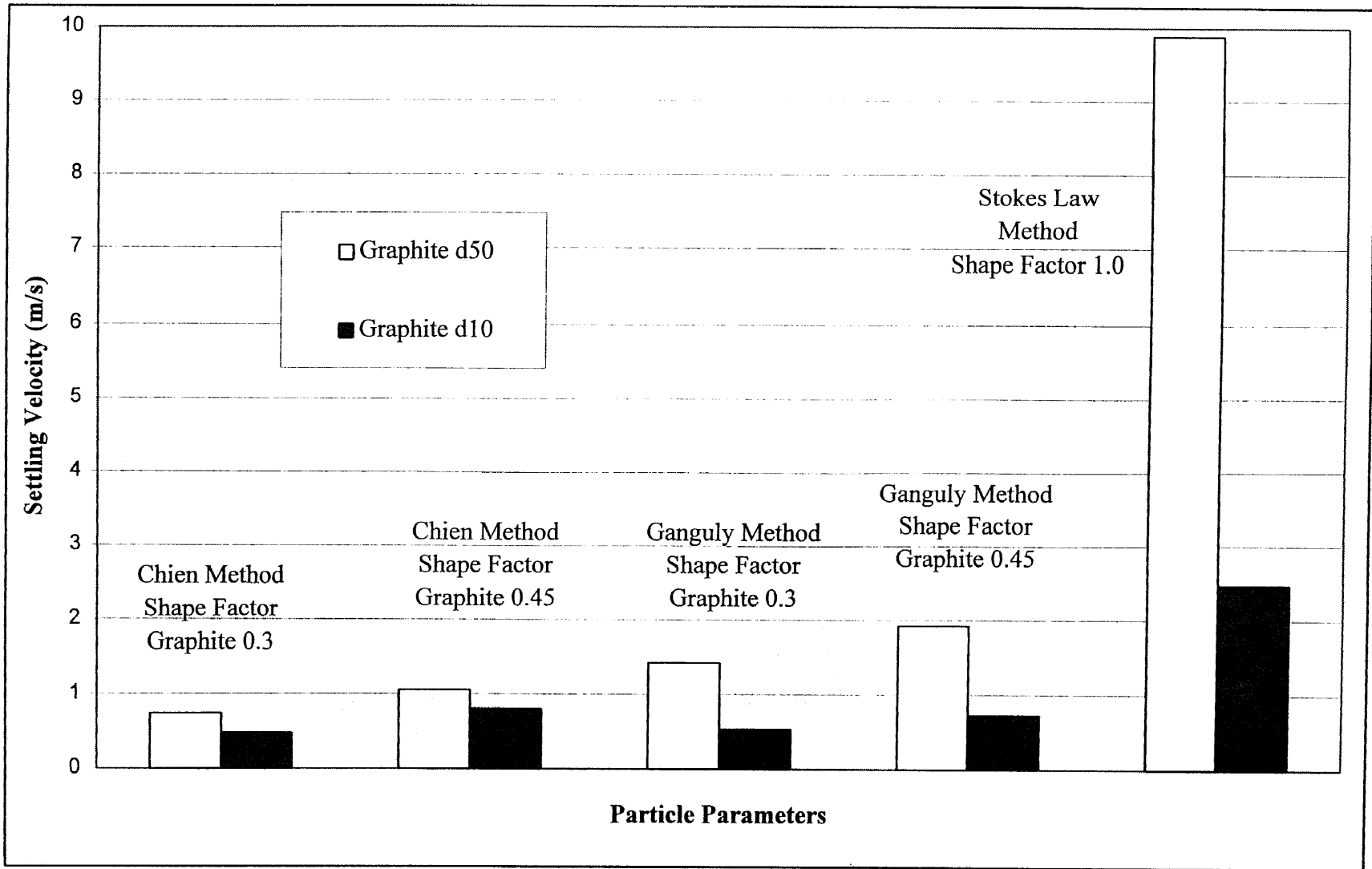
Figure 5.4 Comparison of Settling Velocities for Graphite
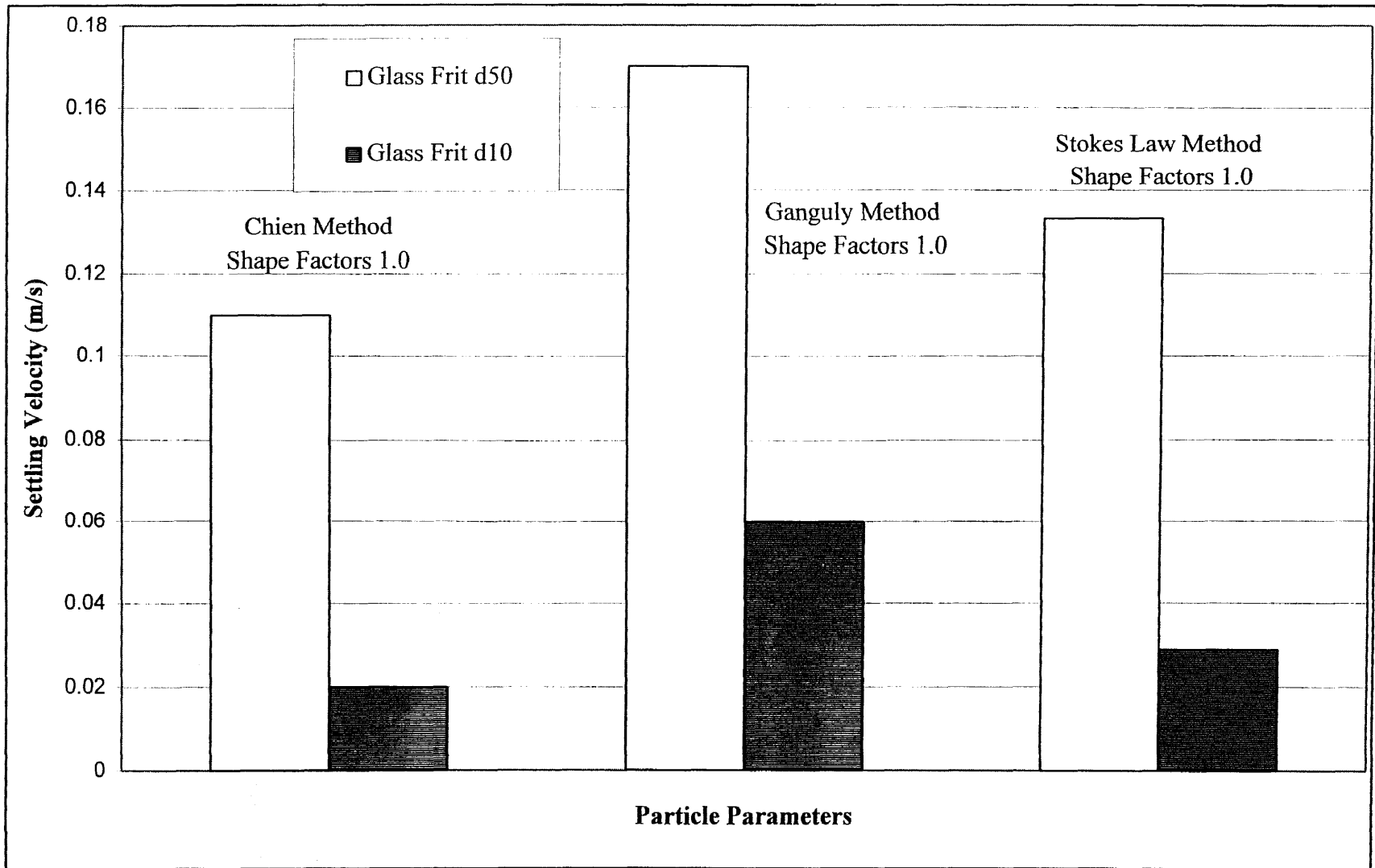
Figure 5.5 Comparison of Settling Velocities for Glass Frit

5.3 Media Transport Through Formation Interstices

The final approach of ISV starter path distribution investigated in this study was transport through the pore spaces or interstices of the formation. Interstitial transport was analyzed using a porous media filtration method to determine particle penetration distance and the degree of surface caking.

5.3.1 Porous Media

5.3.1.1 Background and Development

This approach was based on a study by McDowell-Boyer et al. (1986) which identified three basic mechanisms that can limit particle migration through soil: surface caking, straining and physical and chemical processes. Surface caking occurs when the particles do not penetrate into the media, but instead build up at the soil surface. Straining is the entrapment of particles in the smaller pore spaces, while the larger pore spaces remain open. If straining occurs near the surface, it also may lead to development of a surface mat since the pore openings become restricted. Physical and chemical processes can also remove very small particles relative to the porous media by forces between the particle and the media.

Since particle sizes of the graphite/glass frit are similar to that of the pore spaces, physical and chemical removal processes were eliminated as a possible transport mechanism. Therefore, only the first two methods, surface caking and straining, were explored.

Sakthivadivel (1969) performed laboratory studies on particle capture by filling a 45 cm (18 in.) column with large plastic particles and mineral oil to minimize particle to particle and particle to media interactions. The most critical factor in determining straining within porous media was the ratio of media diameter to the particle diameter, d_m/d_p. For d_m/d_p less than 10, no particle penetration into the media was observed. Thus, surface filtration limited particle penetration. In the range of $10<d_m/d_p<20$, permeability was reduced by a factor of 7-15 with 30% of the pore volume occupied by the deposited particles. When $d_m/d_p>20$, 2-5% of the pore volumes were occupied by the particles and reduced permeability 10-50%.

In another similar study, Sherard et al. (1984) found that finer sand would not penetrate coarser sand during water flow or vibration if $d_{m15}/d_{p85}<9$, where 15% by weight of the coarse filter media had a diameter less than or equal to d_{m15} and 85% by weight of the finer sand particles had diameters less than or equal to d_{p85}. This was based on experiments over a range in d_{m15} from 1 to 10 mm (0.04 to 0.4 in.).

5.3.1.2 Results

Table 5.9 summarizes particle size ratios which were calculated using the Hanford Formation as the filter media, and the graphite/glass frit material as the filtered particle. Two different grain size distributions were assumed for the Hanford Formation soils. Gradation A was based on the overall distribution presented in Figure 3.1, and Gradation B considered only the material passing the No. 4 sieve. As indicated in Table 5.9, all

values are less than 9, which suggests that surface caking will predominate, and penetration of the graphite/glass frit will be minimal.

Although interstitial transport is not a viable method of distributing a conductive lens into the Hanford Formation, it does have significant implications to fracture propagation and dry media transport. The particle straining and surface caking that is likely to occur in the formation should effectively seal the upper and lower boundaries of the fracture to prevent the leakoff of air. The decrease in leakoff would increase the radius of fracture propagation and elevate velocity, thereby enhancing particle transport in the fracture.

Table 5.9 Penetration of Coarser Particles by Finer Particles

Soil Type	d_{m15} (mm)	d_{p85} (mm)	d_{m15}/d_{p85}		
			Graphite 1501	Graphite 205	Glass frit
Hanford - A (Total sample)	0.25	Graphite 1501-0.6 Graphite 205-0.075 Glass Frit-0.075	0.42	3.33	3.33
Hanford - B (minus No. 4)	0.16		0.26	2.13	2.13

5.4 Summary of Model Analysis

This chapter presented several model analyses which were used to estimate fracture dimensions and investigate mechanisms of dry media transport. These are two key

factors in the success of integrating ISV and PF. These model analyses were also used to extrapolate the results of the bench scale study to a full scale application. This section summarizes the results of the model analyses.

Fracture dimensions were estimated by evaluating pressure and velocity distributions in the fracture. Reasonable field parameters were used in development of the distribution models, and results showed that fracture radii of at least a few meters are likely. The fracture initiation pressure in the Hanford Formation is estimated to be at 40 psi (276 kPa) and the maintenance pressure is expected to remain relatively constant throughout the fracture radius. Injection flowrate was found to be the primary factor in fracture propagation and radius determination in this porous formation. Furthermore, the model results suggested that fracture propagation would be minimal if the injection is conducted in a zone with a high pneumatic conductivity.

Entrainment velocities for the starter media estimated using the Shields diagram method for laminar conditions were similar: 0.35 m/s (1.15 ft/sec) for graphite and 0.28 m/s (0.92 ft/sec) for glass frit. Thus, segregation would not be expected using these results. The dust transport method, however, yielded results that differed more than an order of magnitude: 1.2 m/s (3.94 ft/sec) for graphite and 0.14 m/s (5.51 ft/sec) for glass frit. Overall, the high velocities expected in the fracture should counteract the tendency for the particles to segregate. The Shields diagram method results are considered more reliable due to number of difficult assumptions that must be made in the dust transport method.

The final model analysis in this chapter investigated the potential for interstitial transport. The d_{m15}/d_{p85} ratios for the graphite particles averages 0.34, and the ratio for the glass frit particles averages 2.73. Since the ratios for the graphite and the glass frit were significantly less than the straining threshold value of nine, interstitial transport is not expected to be an effective transport mode for the starter path media. In addition to significantly inhibiting particle penetration, surface caking is expected to enhance fracture propagation by sealing the fracture and reducing leakoff of air.

CHAPTER 6

CONCLUSIONS AND RECOMMENDATIONS

The following conclusions and recommendations have been developed based on the results of laboratory testing, bench scale testing, and system modeling.

6.1 Conclusions

Overall, this study has shown that pneumatic fracturing and ISV can be successfully integrated at laboratory bench scale. A pneumatic injection system was developed which is capable of injecting dry media into laboratory test tanks to form a continuous, conductive plane below the soil surface.

1) The Hanford Formation is significantly different from other geologic formations which have been pneumatically fractured to date. Laboratory analysis of test samples show its predominant textural components are gravel and sand with a USCS classification of GP. It contains only 3.4 wt% of non-cohesive fines, and 0.12 wt% organic matter. The hydraulic conductivity of the formation is estimated to be in the range of 1,000 to 10,000 ft/day (0.352 to 3.52 cm/s). A surrogate test soil was developed to simulate the Hanford Formation soil by matching the grain size distribution and gross mineralogy. All bench scale tests were performed using the surrogate test soil.

2) A total of 44 fracture tank tests were performed in Plexiglas test tanks filled with the surrogate soil. The effects of several experimental parameters on the effectiveness of fracturing were studied including moisture content, soil density and injection pressure. The tests were subject to scale limitations including wall effects and simulated surcharge. However, quantitative extrapolation of injection pressures, flows, and fracture dimensions to full scale applications should be approached with caution.

3) Soil density was determined to have a significant effect on the ability to attain a discrete fracture. Dry density for the tests was varied from 103 to 112.8 lb/ft^3 (1.65 to 1.81 g/cm^3). Fracturing above 105 lb/ft^3 (1.68 g/cm^3) was generally successful. Below that value inconsistencies were observed, although two successful fractures were obtained at densities as low as 103 lb/ft^3 (1.65 g/cm^3). While the actual field density of the soil at the proposed test site is not known, reconnaissance data suggest it will be at the lower end of the density range used for the laboratory tests.

4) Moisture content was also determined to have a significant role on the ability to obtain a discrete fracture in the soil, and to subsequently inject dry media into the fracture. Tests were performed at moisture contents ranging from 0.8 wt% to 7.8 wt%. Fracturing at the higher moisture contents was generally successful. However, inconsistencies in fracture behavior were observed below 2 wt% moisture. The experimental difficulties at the lower moisture contents were attributed to reduction of interstitial surface tension, and a corresponding loss of

apparent soil cohesion. While the actual moisture content at the proposed test site is not known and will obviously vary with season and precipitation events, reconnaissance data suggest the field moisture content may be expected to range from 1 to 3 wt%.

5) There appears to be an interactive relationship between soil moisture and density. For example, successful fracture injections were made with combinations of high moisture content and low density, as well as the reverse. However, more inconsistencies were observed when both density and moisture were held low.

6) The starter path media, consisting of graphite and glass frit, was successfully injected during two separate tank tests to form a conductive link between two electrodes spaced 12 in. (30.5 cm) apart (Most injection testing was performed with plain air or silica sand to minimize contamination of surrogate soil). The conductive lenses averaged 4 in. (10.2 cm) in thickness, and conductivity tests showed an average resistance of 0.80 ohms across graphite electrodes and 120 ohms across aluminum electrodes.

7) The observed soil fracture mechanisms in the coarse-grained Hanford Formation soils appear somewhat different than the cohesive soils and rock normally treated with the pneumatic fracturing technology. Although the presence of moisture in these naturally non-cohesive soils will provide some apparent cohesion, it is speculated that the formation may not "fracture" in the normal brittle sense and will generally rebound more elastically than the cohesive soils and rock. Instead, the primary mechanism might be better described as "pneumatic intrusion" or

"pneumatic cutting." This behavior, coupled with the high leakoff of injected air into the unfractured parts of the formation, indicate that higher than normal flows and pressures will be required to attain a fracture in this formation.

8) The rate of successful fractures was shown to improve by the addition of a surcharge to the bench scale tests, although only 20% of the expected field overburden could be applied to the small scale system. Thus, during the field demonstration, it is speculated that the overburden weight at the proposed injection depth of 16 ft (5 m) will improve fracture conditions, especially, if the field density and moisture content are in the low end of the range tested in the bench scale study.

9) Horizontal infiltrometer tests were conducted to examine the ability of the graphite and glass frit media to penetrate the unfractured soil matrix by interstitial transport. Experiments performed under a variety of conditions with different graphite gradations consistently showed minimal penetration of the conductive media into soil matrix at 0.13 in. (3 mm) maximum in sand pores, and 0.2 in. (5 mm) maximum at boundaries of oversize particles. These test results were verified with filtration and straining criteria for porous media published in the literature. Based upon both the laboratory and theoretical results, interstitial transport is not expected to be a significant transport mechanism in the Hanford Formation, except in locally coarse zones consisting entirely of cobbles and gravel.

10) Bench scale tests showed that some segregation of the graphite from the glass frit particles occurred during injection. However, the degree of segregation is not expected to adversely affect melt initiation. The results did indicate, however, that

a significant amount of particle straining and surface caking was occurring which reduced permeability at the fracture boundaries. These mechanisms are expected to be beneficial for fracture propagation in this coarse grained formation.

11) A mathematical model for applying the PF/ISV concept to the Hanford Formation was developed using a radial injection approach. Model results showed that leakoff of injected air into the coarse formation soils is considerable, although an effective radius of several feet appears possible depending on the local formation texture.

12) The ability to keep the graphite/glass frit media suspended in the injection stream and transport it in discrete, planar fractures was modeled using two theoretical approaches. It was found that relatively low air velocities (1.3 ft/sec (0.4 m/s)) are sufficient to keep the mixture suspended, suggesting that transport of the graphite/glass frit mixture should not be a problem in open fractures. The Shields diagram method predicted the entrainment velocities of graphite and glass frit to be 0.35 m/s and 0.28 m/s (0.017 ft/sec and 0.013 ft/sec), respectively. The dust transport method estimated the entrainment velocity of graphite to be 1.2 m/s (0.06 ft/sec) and of the glass frit to be 0.14 m/s (0.007 ft/sec). Even using the dust transport results, the potential for extreme segregation is minimal due to the high injection velocities in the fracture. It is also likely that the lens will incorporate the mixture before significant segregation can occur.

6.2 Recommendations

The following are recommendations for implementing the integration of ISV and PF in the field:

1) Real time conductivity measurements should be taken during starter path injection to better understand the ratio of mass of starter path media to conductivity, as well as to determine whether or not the desired conductivity has been achieved.

2) Real time flow and pressure measurements should be documented to better understand the pneumatic fracturing or "cutting" which occurs in a porous formation. Additionally, a pressure transducer should be used at the nozzle to investigate the fracture initiation pressure for highly permeable formations.

3) A significant volume of air or other inert gas is needed for the dry media injection processes due to the high formation leakoff and long injection duration. The standard PF field trailer may not be sufficient, and a large reservoir such as a compressed gas tube trailer should be considered.

4) The dry media injection process should be terminated near the end of the availability of dry media, as this will reduce the likelihood of air disrupting the continuity of the injected lens.

5) The real time mass flow rates of the dry media should be monitored, and a level indicator system utilized to determine the amount of dry media in the tanks. Alternatively, a continuous feed system would be beneficial to inject an "endless" amount of the dry media.

6) If injection is to be performed into a very coarse region, a thick layer of the starter path is suggested as the cobbles may create many discontinuities in the injected lens. Also, the coarse region should be bounded by a finer layer to prevent excessive "leakoff".

7) A good seal is imperative above the nozzle between the formation and the injector to inhibit "leakoff" around the injector. Suggested method includes a bentonite layer directly above the nozzle followed by a non-shrinking grout to fill the remainder of the borehole.

8) The graphite electrodes should be installed before injecting the starter path material as this will better simulate conductivity behavior during melt initiation.

9) An excavation of the starter path lens should be performed after a full scale injection to permit direct observation of the physical characteristics of the conductive lens.

APPENDIX A

CALCULATION OF PRESSURE DISTRIBUTION

This appendix provides supporting calculations for the pressure distribution

determination in Section 5.1.1.

Pressure distribution calculations are based on the following assumptions:

Q	= 1.42	cubic meters/sec or (3000 cfm)
ν	= $0.14987 \cdot 10^{-4}$	square meters/sec
b	= 0.05	meters
R1	= 0.0762	meters or (3 inches)
R2	= 0.1, 0.5 .. 2.5	meters
P1	= 29978.335	absolute meters air (40 + 14.7 psi)
P2	= 0.0	absolute meters air
g	= 9.81	meters/square sec

1 atm = 14.7 psi = 8056.352 meters of air

1 psi = 548.05 meters of air

The formula used for calculating the pressure at a radial distance takes into

consideration the compressibilty effects. The equation presented in Section 5.1.1

is solved for P(R2) as follows:

$$P(R2) = \frac{\sqrt{P1^2 - \dfrac{12 \cdot P1 \cdot Q \cdot \nu \cdot \ln \dfrac{R2}{R1}}{\pi \cdot g \cdot b^3}} - 8056.352}{548.05}$$

96

APPENDIX A
(Continued)

Plotting the radial pressure (absolute meters of air) at the corresponding radius (m)

results in the following distribution:
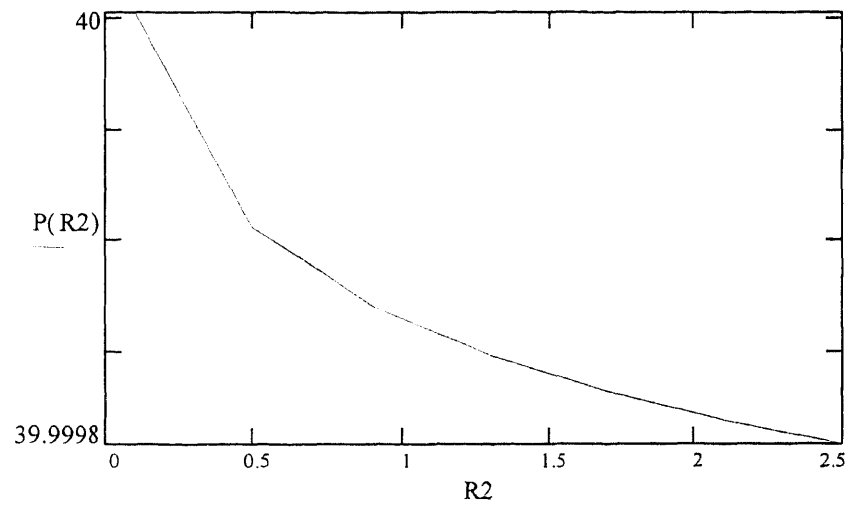
APPENDIX B

CALCULATION OF VELOCITY DISTRIBUTION

A sample velocity distribution calculation, using the model presented in

Figure 5.1, is presented based on the following assumptions:

Q	= 1.42	cubic meters/sec
b	= 0.05	meters
r	= 1,2..4	meters
K	= 0.000007	meters/sec
iu	= 4500	
id	= 1500	

The pneumatic gradient represents an average of the upward and

downward gradients estimated at a depth of 5 m.

Calculation of velocity distribution in the discrete fracture is calculated

from the following equation:
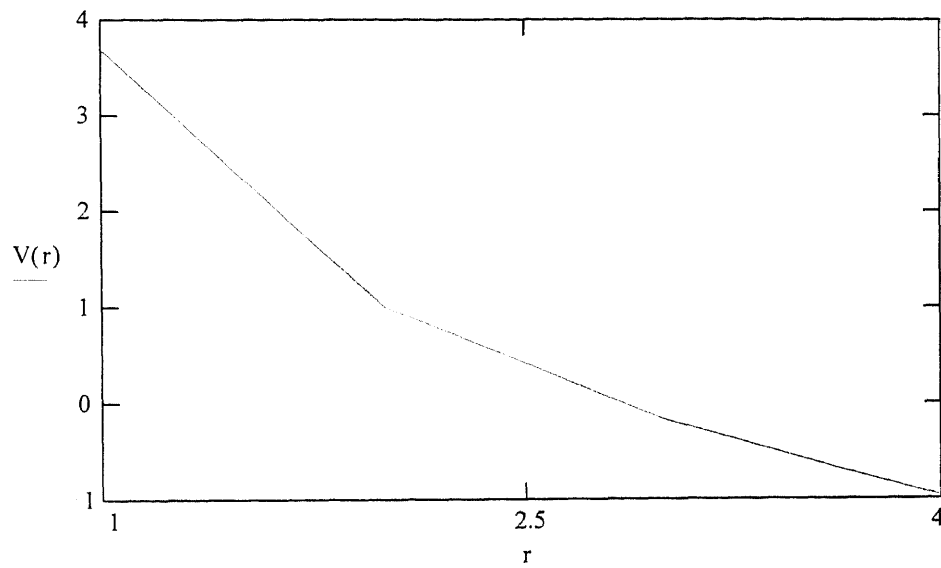
$$Q(r) = \left[K \cdot (iu + id) \cdot 3.14 \cdot \left[(r + 0.5)^2 - (r - 0.5)^2 \right] \right]$$

Solving for the velocity in the discrete fracture at a specified radius:

$$V(r) = \frac{1.42 - \sum_{r=1}^{r} Q(r)}{2 \cdot \pi \cdot r \cdot b}$$

APPENDIX B
(Continued)

Plotting the radial velocity (m/sec) at the corresponding radius (m) results in the

following distribution:

APPENDIX C

CALCULATION OF ENTRAINMENT VELOCITIES

Introduction

This appendix contains supporting calculations for the entrainment velocity determinations in Section 5.2.

Shields Diagram Method

Laminar Case

In the laminar case, the boundary shear stress was defined as:

$$\tau_0 = \mu (dV/dy) \tag{1}$$

where:

μ = dynamic viscosity (M/L-T)

dV/dy = velocity distribution in the vertical direction

Substituting Equation 1 into Equation 5.5, separating dV and dy, and integrating dV from zero to V and dy from zero to one-half the fracture aperture, b/2, the resulting expression for dimensionless shear stress becomes:

$$\tau^* = \frac{2\mu \cdot V}{b \cdot d(\gamma_s - \gamma_f)} \tag{2}$$

where:

b = fracture aperture (L)

Table 1 summarizes these results for both graphite and glass frit over a range of velocities

chosen so that the resulting lines would intersect the Shields diagram.

Table 1 Calculation of Parameters for Shields Method (Laminar Case)

v (m/s)	Re_{gf-d10}	Re_{gf-d50}	Re_{gr-d10}	Re_{gr-d50}	τ_{gf-d10}	τ_{gf-d50}	τ_{gr-d10}	τ_{gr-d50}
0.1	0.01	0.022	0.103	0.206	1.77	0.71	0.18	0.08
0.2	0.015	0.031	0.146	0.291	3.54	1.41	0.35	0.15
0.3	0.018	0.038	0.178	0.357	5.31	2.12	0.53	0.23
0.4	0.021	0.044	0.206	0.412	7.09	2.83	0.71	0.30
0.5	0.023	0.05	0.23	0.461	8.86	3.53	0.89	0.38
0.6	0.025	0.054	0.252	0.504	10.63	4.24	1.06	0.46
0.7	0.027	0.059	0.272	0.545	12.40	4.94	1.24	0.53
0.8	0.029	0.063	0.291	0.583	14.17	5.65	1.42	0.61
0.9	0.031	0.066	0.309	0.618	15.94	6.36	1.59	0.68
1.0	0.033	0.07	0.326	0.651	17.71	7.06	1.77	0.76

The following grain sizes were used for the graphite (gr) and the glass frit (gf) based on laboratory tests and manufacturer's data:

$d_{gr}10 = 0.0002$ m

$d_{gr}50 = 0.0004$ m

$d_{gf}10 = 0.00002$ m

$d_{gf}50 = 0.000043$ m

Other physical characteristics assumed were:

$b = 0.05$ m

$\mu = 1.8 \times 10^{-5}$ kg/m-s @ 20°C

$v = 1.5 \times 10^{-5}$ m^2/s @ 20°C

$\gamma_{gr} = 2040$ kg/m^3

$\gamma_{gf} = 2380$ kg/m^3

$\gamma_f = 1.213$ kg/m^3

The results of Table 1 were then plotted on the Shields diagram as depicted in Figure 5.3. The resulting entrainment velocities for the graphite and glass frit are summarized in Table 5.2.

Turbulent Case

The turbulent case for the Shields method was also examined. In the turbulent condition, the boundary shear stress has an extra parameter, the eddy viscosity, η (Boggs, 1987). This results in the following changes to Equations (1), (2), and (5.8), respectively:

$$\tau_0 = (\mu + \eta) dV/dy \qquad (3)$$

$$\tau^* = \frac{2(\mu + \eta) \cdot V}{b \cdot d(\gamma_s - \gamma_f)} \qquad (4)$$

$$R_{eg} = \frac{\sqrt{\dfrac{2(\mu + \eta) \cdot V}{b \cdot \rho}} \cdot d}{\nu} \qquad (5)$$

Note that the term $(\mu + \eta)/\rho$ equals $(\nu + \varepsilon)$ used in the dust transport model, the next model to be discussed. Therefore, η was calculated using the expression $\eta = \varepsilon \cdot \rho$, where ε is the coefficient of turbulent exchange. The coefficient of turbulent exchange is defined by:

$$\varepsilon = \alpha \cdot U_f \cdot k \cdot Z \qquad (6)$$

where:

$$Z = b$$

The assumptions made to arrive at this equation will be discussed later.

The same procedure used to estimate the entrainment velocities in the laminar flow case was used for the turbulent flow case. Table 2 contains the calculated values of τ^* and R_{eg} for the range 0.1 to 1.0 m/s. When these values are plotted on the Shields diagram, a shift well above the characteristic curve is noted as shown in Figure C.1.

Table 2 Calculated Parameters for Shields Method (Turbulent Case)

v (m/s)	$Re_{gf\text{-}d10}$	$Re_{gf\text{-}d50}$	$Re_{gr\text{-}d10}$	$Re_{gr\text{-}d50}$	$\tau_{gf\text{-}d10}$	$\tau_{gf\text{-}d50}$	$\tau_{gr\text{-}d10}$	$\tau_{gr\text{-}d50}$
0.1	0.14	0.30	7.92	15.84	323.05	128.78	1047	448.81
0.2	0.20	0.42	11.20	22.40	646.10	257.56	2095	897.62
0.3	0.24	0.52	13.72	27.43	969.15	386.34	3142	1346
0.4	0.28	0.60	15.84	31.67	1292	515.12	4189	1795
0.5	0.31	0.67	17.71	35.41	1615	643.90	5237	2244
0.6	0.34	0.73	19.40	38.79	1938	772.68	6284	2693
0.7	0.37	0.79	20.95	41.90	2261	901.46	7331	3142
0.8	0.39	0.85	22.40	44.79	2584	1030	8378	3590
0.9	0.42	0.90	23.75	47.51	2907	1159	9426	4039
1.0	0.44	0.95	25.04	50.08	3231	1288	1047	4488

By extending the data lines to the extrapolated characteristic curve, the corresponding Reynolds grain numbers were obtained by dropping a vertical line from the intersection of the data lines and the Shields diagram. Rearranging Equation (5), the critical entrainment velocity can be obtained by:

$$V = \frac{R_{eg}^2 \cdot v^2 \cdot b}{2d^2 \cdot (v + \varepsilon)} \qquad (7)$$

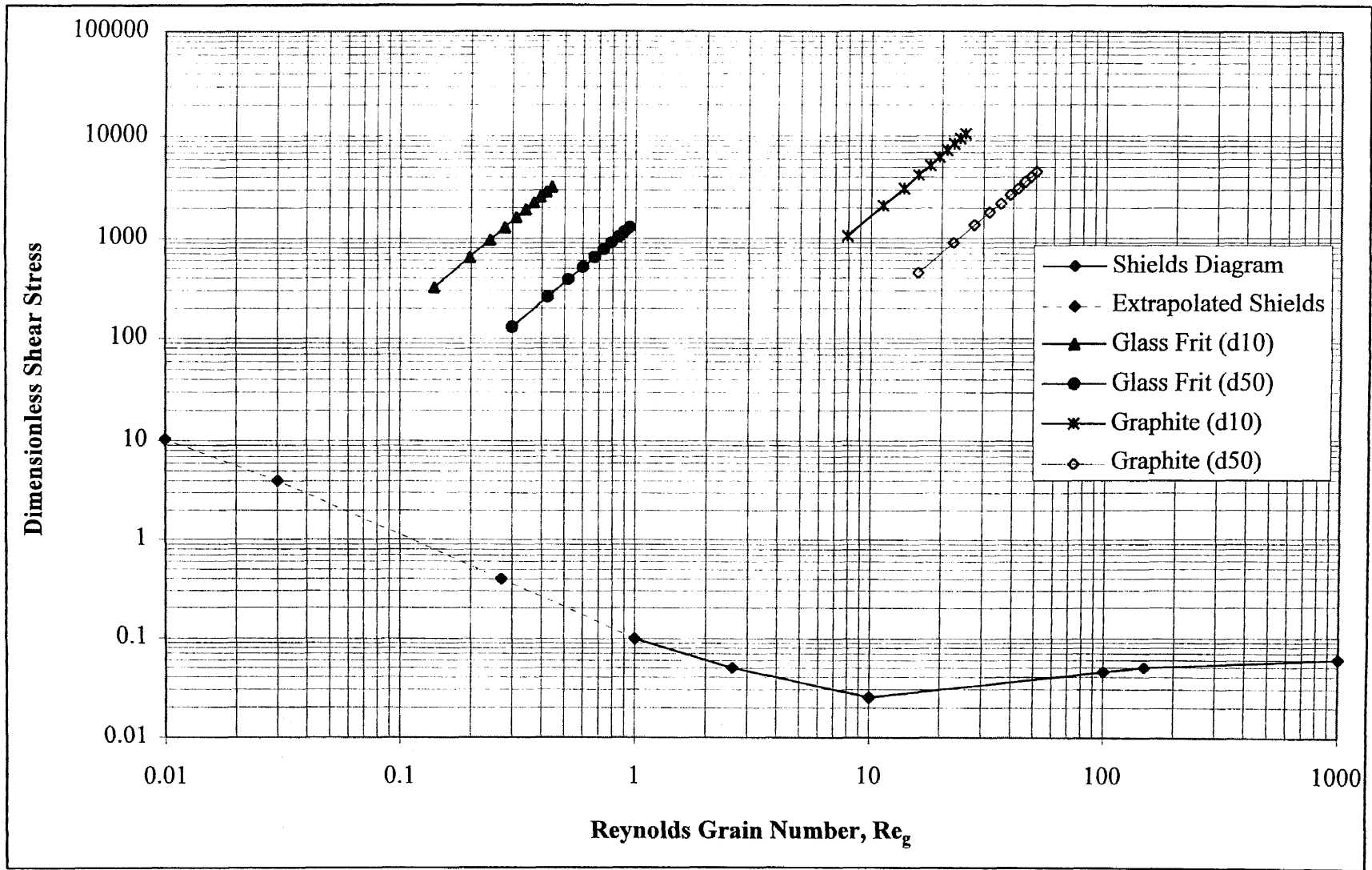The resulting entrainment velocities for the turbulent case are shown in Table 3.

Figure C.1 Shields Diagram Method (Turbulent Flow)

Table 3 Entrainment Velocities by Shields Method (Turbulent Case)

Particle diameter (m)		Reynolds grain number	Coefficient of Turb. Ex., ε (m^2/s)	Entrainment Velocity, V (m/s)
$d_{gr}10$	0.0002	0.19	0.025	2.03×10^{-4}
$d_{gr}50$	0.0004	0.39	0.099	5.39×10^{-3}
$d_{gf}10$	0.00002	0.019	0.0003	1.61×10^{-2}
$d_{gf}50$	0.000043	0.03	0.0013	2.08×10^{-3}

A comparison with results in Table 5.2 show the turbulent entrainment velocities to be a few orders of magnitude lower than the laminar values. The velocity of the turbulent case is expected to be lower than the laminar case due to eddying effects. The magnitude of the difference appears excessive, and may be due to the inability to accurately estimate the coefficient of turbulent exchange.

Dust Transport Method

<u>Turbulent Case</u>

Again, note that $v = \mu/\rho$ and $\varepsilon = \eta/\rho$. Therefore, $(v+\varepsilon)=(\mu+\eta/\rho)$ as mentioned in the Shields diagram method. As discussed in Section 5.2.2.2, the mixing length, l, in Equation 5.12 is equal to the product of the height above the ground and the von Karman constant. The coefficient of turbulent exchange, ε, is then expressed as:

$$\varepsilon = \alpha \sqrt{w'^2}\, kz \qquad (8)$$

where:

$\alpha = 1$ for stable atmospheres

k = 0.4 (von Karman constant)

z = height above boundary layer (b/2)

$\sqrt{\overline{w'^2}}$ = force opposing particle settling

Tsoar and Pye (1987) assumed that $U_f / \sqrt{\overline{w'^2}}$ = 0.06 in their study of long distance dust transport. The assumption accounted for the high probability that at this ratio, a particle may be carried to a height well above the ground. For transport in a fracture, where the particle lift height is minimal, the ratio is assumed to be $\sqrt{\overline{w'^2}}$ = U_f. The resulting expression for the coefficient of turbulence is ε = 0.4·U_f·z. Note that setting α = 1, which assumes that the atmosphere in the fracture is stable, is an uncertainty.

The settling velocities calculated by Stokes Law for the different size parameters and the corresponding coefficients of turbulent exchange are shown in Table 5.4.

Chien Method

The values in Table 5.5 were calculated in English units and then converted to SI units. The values were:

μ = 1.8 x 10^{-2} centipoise

ρ_f = 0.01 lb/gallon for air

ρ_p = 17.03 for graphite, 19.9 for glass frit

The results are displayed in Table 5.6. All of these calculations are shown in Plates C.1 through C.4.

PLATE C.1

Calculations for Settling Velocity and Reynolds Grain number

Using Chien method

<u>Glass frit (d10)</u>

$\mu = 1.8 \cdot 10^{-2}$ (cp)

d $= 0.00079$ (in)

ρf 0.01 (lb/gal)

ρp 19.9 (lb/gal)

<u>For shape factor of 1.0</u>

$$Vs \quad 0.0002403 \cdot \exp(5.030) \cdot \frac{\mu}{d \cdot (\rho f)} \cdot \left[1 - 920790.49 \cdot \exp(-5.030) \cdot d \cdot \left(\frac{\rho p}{\rho f} - 1 \right) \cdot \frac{d \cdot \rho f}{\mu}^2 - 1 \right]$$

Vs $= 0.076$ (ft/s)

$$Reg \quad \frac{927.64 \cdot d \cdot Vs \cdot \rho f}{\mu}$$

Reg $= 0.031$

PLATE C.2

Calculations for Settling Velocity and Reynolds Grain number

Using Chien method

Glass frit (d50)

$\mu = 1.8 \cdot 10^{-2}$ (cp)

$d = 0.0017$ (in)

$\rho f = 0.01$ (lb/gal)

$\rho p = 19.9$ (lb/gal)

For shape factor of 1.0

$$Vs = 0.0002403 \cdot \exp(5.030) \cdot \frac{\mu}{d \cdot (\rho f)} \cdot \left[1 + 920790.49 \cdot \exp(-5.030) \cdot d \cdot \left(\frac{\rho p}{\rho f} - 1 \right) \cdot \frac{d \cdot \rho f}{\mu}^2 - 1 \right]$$

$Vs = 0.352$ (ft/s)

$$Reg = \frac{927.64 \cdot d \cdot Vs \cdot \rho f}{\mu}$$

$Reg = 0.308$

PLATE C.3

Calculations for Settling Velocity and Reynolds Grain number
Using Chien method

<u>Graphite (d10)</u>

$\mu = 1.8 \cdot 10^{-2}$ (cp)

$d = 0.008$ (in)

$\rho f = 0.01$ (lb/gal)

$\rho p = 17.03$ (lb/gal)

<u>For shape factor of 0.3</u>

$$Vs = 0.0002403 \cdot \exp(5.030 \cdot 0.3) \cdot \frac{\mu}{d \cdot (\rho f)} \cdot \left[\sqrt{1 + 920790.49 \cdot \exp(-5.030 \cdot 0.3) \cdot d \cdot \left(\frac{\rho p}{\rho f} - 1\right) \cdot \frac{d \cdot \rho f}{\mu}}\right]$$

$Vs = 1.581$ (ft/s)

$$Reg = \frac{927.64 \cdot d \cdot Vs \cdot \rho f}{\mu}$$

$Reg = 6.52$

<u>For a shape factor of 0.45</u>

$$Vs = 0.0002403 \cdot \exp(5.030 \cdot 0.45) \cdot \frac{\mu}{d \cdot (\rho f)} \cdot \left[\sqrt{1 + 920790.49 \cdot \exp(-5.030 \cdot 0.45) \cdot d \cdot \left(\frac{\rho p}{\rho f} - 1\right) \cdot \frac{d \cdot \rho f}{\mu}}\right]$$

$Vs = 2.169$ (ft/s)

$$Reg = \frac{927.64 \cdot d \cdot Vs \cdot \rho f}{\mu}$$

$Reg = 8.944$

PLATE C.4

Calculationsfor Settling Velocity and Reynolds Grain number

Using Chien method

Graphite (d50)

$\mu \ = 1.8 \cdot 10^{-2}$ (cp)

$d \ = 0.016$ (in)

$\rho f \ = 0.01$ (lb/gal)

$\rho p \ \ 17.03$ (lb/gal)

For shape factor of 0.3

$$Vs \ = 0.0002403 \cdot \exp(5.030 \cdot 0.3) \cdot \left[\frac{\mu}{d \cdot (\rho f)} \right] \cdot \sqrt{1 + 920790.49 \cdot \exp(-5.030 \cdot 0.3) \cdot d \cdot \left(\frac{\rho p}{\rho f} - 1 \right) \cdot \frac{d \cdot \rho f}{\mu}}$$

$Vs = 2.44$ (ft/s)

$$Reg \ \ \frac{927.64 \cdot d \cdot Vs \cdot \rho f}{\mu}$$

$Reg = 20.116$

For a shape factor of 0.45

$$Vs \ = 0.0002403 \cdot \exp(5.030 \cdot 0.45) \cdot \left[\frac{\mu}{d \cdot (\rho f)} \right] \cdot \sqrt{1 + 920790.49 \cdot \exp(-5.030 \cdot 0.45) \cdot d \cdot \left(\frac{\rho p}{\rho f} - 1 \right) \cdot \frac{d \cdot \rho f}{\mu}}$$

$Vs = 3.481$ (ft/s)

$$Reg \ = \frac{927.64 \cdot d \cdot Vs \cdot \rho f}{\mu}$$

$Reg = 28.7$

Ganguly Method

The first step in using this method was to calculate the Archimedes number using Equation 5.17. Next, the Reynolds grain numbers were calculated by Equation 5.18 using the same shape factors used in the Chien method. The results of the Archimedes number and Reynolds grain number are presented in Table 5.

Table 5 Calculations of parameters for Ganguly Method

Particle/Parameter	Shape Factor	Archimedes No.	Reynolds grain number
Graphite/d_{50}	0.3	4791	38.2
Graphite/d_{50}	0.45	4791	51.7
Graphite/d_{10}	0.3	598.8	7.2
Graphite/d_{10}	0.45	598.8	9.7
Glass Frit/d_{50}	1	6.9	0.5
Glass Frit/d_{10}	1	0.7	0.08

Using the standard definition for the Reynolds grain number in Equation (9), the settling velocity was derived as shown in Equation 5.19. Results of the settling velocities are shown in Table 5.8.

$$R_{eg} = \frac{d \cdot U_f \cdot \rho_f}{\mu} \qquad (9)$$

Following the same procedure as the Chien method, the settling velocities in Table 5.7 were substituted into the dust transport method to determine the entrainment velocities. The resulting entrainment velocities are displayed in Table 5.8. Detailed calculations using the Ganguly method are shown in Plate C.5. Although the shape factors for these results are not in the range for use of the Ganguly equation, they are

PLATE C.5

Calculations for Settling Velocity and Reynolds Grain Number
Using Ganguly Method

dgr50 = 0.0004	(m)	$\rho f = 1.213$	(kg/m^3)
dgf10 = 0.00002	(m)	$\rho gr = 2040$	(kg/m^3)
dgf50 = 0.000043	(m)	$\rho gf = 2380$	(kg/m^3)
dgr10 = 0.0002	(m)	$\mu = 1.8 \cdot 10^{-5}$	(kg/m-s)

$$g = 9.807 \quad (m/s^2)$$

Graphite (d50)

$$Ar \quad \frac{dgr50^3 \cdot g \cdot \rho f \cdot (\rho gr \quad \rho f)}{\mu^2}$$

$$Ar = 4.791 \cdot 10^3$$

Shape Factor of 0.3

$$Reg \quad 0.103 \cdot Ar^{0.804} \cdot 0.3^{0.745}$$

$$Reg = 38.224$$

$$Vs \quad \frac{Reg \cdot \mu}{dgr50 \cdot \rho f}$$

$$Vs = 1.418 \quad (m/s)$$

Shape Factor of 0.45

$$Reg \quad 0.103 \cdot Ar^{0.804} \cdot 0.45^{0.745}$$

$$Reg = 51.704$$

$$Vs \quad \frac{Reg \cdot \mu}{dgr50 \cdot \rho f}$$

$$Vs = 1.918 \quad (m/s)$$

PLATE C.5
(Continued)

Graphite (d10)

$$Ar = \frac{dgr10^3 \cdot g \cdot \rho f \cdot (\rho gr - \rho f)}{\mu^2}$$

$Ar = 598.844$

Shape Factor of 0.3

$Reg = 0.103 \cdot Ar^{0.804} \cdot 0.3^{0.745}$

$Reg = 7.182$

$$Vs = \frac{Reg \cdot \mu}{dgr10 \cdot \rho f}$$

$Vs = 0.533$ (m/s)

Shape Factor of 0.45

$Reg = 0.103 \cdot Ar^{0.804} \cdot 0.45^{0.745}$

$Reg = 9.715$

$$Vs = \frac{Reg \cdot \mu}{dgr10 \cdot \rho f}$$

$Vs = 0.721$ (m/s)

Glass frit (d50)

$$Ar = \frac{dgf50^3 \cdot g \cdot \rho f \cdot (\rho gf - \rho f)}{\mu^2}$$

$Ar = 6.944$

Shape Factor of 1.0

$Reg = 0.103 \cdot Ar^{0.804} \cdot 1.0^{0.745}$

$Reg = 0.489$

$$Vs = \frac{Reg \cdot \mu}{dgf50 \cdot \rho f}$$

$Vs = 0.169$ (m/s)

PLATE C.5
(Continued)

Glass frit (d10)

$$Ar = \frac{dgf10^3 \cdot g \cdot \rho f \cdot (\rho gf - \rho f)}{\mu^2}$$

Ar = 0.699

Shape Factor of 1.0

Reg = $0.103 \cdot Ar^{0.804} \cdot 1.0^{0.745}$

Reg = 0.077

$$Vs = \frac{Reg \cdot \mu}{dgf10 \cdot \rho f}$$

Vs = 0.057   (m/s)

similar to the results of the Chien method. A comparison of the settling velocities using the three methods for graphite particles is displayed in Figure 5.4, and for glass frit in Figure 5.5.

Laminar flow

The laminar case was calculated in the same manner as the turbulent flow case, but the coefficient of turbulent exchange was excluded. Note that this is not normally part of the dust transport method, but the analysis was made in an effort to correlate this method with the laminar flow case. The resulting expression for entrainment velocity is:

$$V = \frac{U_f^2 \cdot b}{2v} \tag{10}$$

By substituting the Stokes Law settling velocities into Equation (10), the entrainment velocities were calculated, and are presented in Table 6.

Table 6 Entrainment Velocities by Dust Transport Method-Laminar (Stokes Law)

Size parameter	$V_{graphite}$ (m/s)	$V_{glass\ frit}$ (m/s)
d10	10,173	1.05
d50	162,385	25.42
2/3 d10	2,056	--------
2/3 d50	32,278	--------

using $v = 1.5 \times 10^{-5}$ m^2/s.

Similarly, the laminar results for the Chien and Ganguly methods are presented in Table 7 and Table 8, respectively.

Table 7 Entrainment Velocities by Dust Transport Method-Laminar (Chien method)

Particle/Parameter	Shape Factor	Settling Velocity, U_f (m/s)	Entrainment Velocity, V (m/s)
Graphite/d_{50}	0.3	0.74	912.65
Graphite/d_{50}	0.45	1.06	1872.66
Graphite/d_{10}	0.3	0.48	384.0
Graphite/d_{10}	0.45	0.8	1066.66
Glass frit/d_{50}	1.0	0.11	20.17
Glass frit/d_{10}	1.0	0.02	0.67

Table 8 Entrainment Velocities by Dust Transport Method-Laminar (Ganguly method)

Particle/Parameter	Shape Factor	Settling Velocity, U_f (m/s)	Entrainment Velocity, V (m/s)
Graphite/d_{50}	0.3	1.42	3360.67
Graphite/d_{50}	0.45	1.92	6144.0
Graphite/d_{10}	0.3	0.53	468.17
Graphite/d_{10}	0.45	0.72	864.0
Glass frit/d_{50}	1.0	0.17	48.17
Glass frit/d_{10}	1.0	0.06	6.0

Conclusion

This appendix has presented the intermediate calculations for the Shields method and the dust transport method. Additionally, the results of adapting each method to consider another flow regime were presented. The purpose of the modifications was to compare the two methods for laminar and turbulent cases.

The Shields method was used to study the turbulent flow case by incorporating the coefficient of turbulent exchange into the laminar method. The resulting entrainment

velocities were three orders of magnitude less than the laminar case entrainment velocities using the Shields method shown in Section 5.2. Comparing the turbulent results from the Shields method to the dust transport method revealed a difference of 3 to 5 orders of magnitude for graphite and one order of magnitude difference for glass frit.

Similarly, the dust transport method was modified to study the laminar case by subtracting the coefficient of turbulent exchange. The entrainment velocities for the laminar case were three orders of magnitude larger than the turbulent case using the dust transport method. The laminar results of the dust transport method were also 3 to 4 orders of magnitude greater than the laminar results of the Shields method for graphite and 1 to 2 orders of magnitude greater for glass frit.

The large difference between the two methods for the same flow regime suggest that adapting either method to another flow regime is quite complex, and requires further study. At present, it is recommended that the Shields method be used to estimate entrainment velocities for the laminar case, and the dust transport method should be used for the turbulent case.

APPENDIX D

SHAPE FACTOR DETERMINATION

The shape factors for the graphite particles were chosen by visual observation. The glass frit particles were assumed to be spherical since they are sufficiently small in accordance with Stokes Law.

The observations of the graphite particles were compared to Figure D.1, using estimations of the axes length ratios, D_S/D_I and D_I/D_L, which stand for the short (D_S), intermediate (D_I), and long (D_L) axes. Estimates for the short axis to intermediate axis ratio, D_S/D_I, ranged between 0.05 and 0.10, while the values for the intermediate axis to long axis ratio, D_I/D_L, ranged from 0.67 to 0.90. Note that a range of shape factors was selected to account for observation error. For the given ratios, a range of 0.3 to 0.45 was determined using Figure D.1.
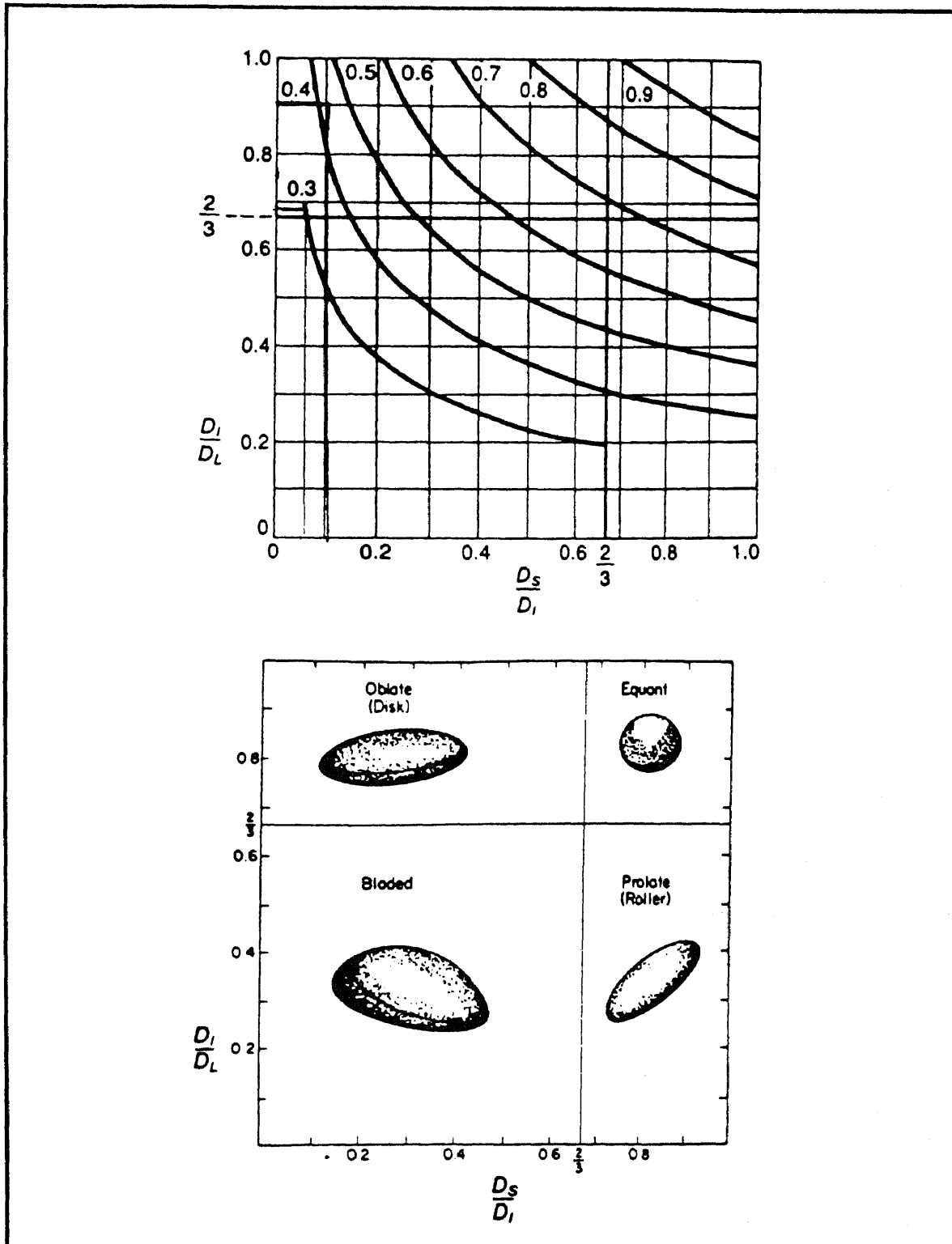
Figure D.1 Sphericity Determination Chart (Boggs, 1987)

APPENDIX E

DESCRIPTION OF INJECTED MEDIA

This appendix describes the various media used in the laboratory tests. Table E.1 and

Figure E.1 summarize the grain size characteristics of the media for the conductivity tests

(Section 4.2) and the horizontal infiltrometer tests (Section 4.3).

Table E.1 Description of Injected Media

Media	Manufacturer	Description
Graphite 205	Cummings-Moor Co.,	85% passes No. 200 sieve
Graphite 635	Dixon Ticonderoga Co.,	75% passes No. 200 sieve
Graphite 1501	Superior Graphite Co.,	See Figure E.1
Glass Frit	American Ceramic Products, Inc.	See Figure E.1

The grain size distribution for the Graphite 1501 was based on data provided by Superior

Graphite Co. in their product data sheet which is also included in this appendix. The

grain size distribution for the glass frit was determined in the HSMRC Laboratory via
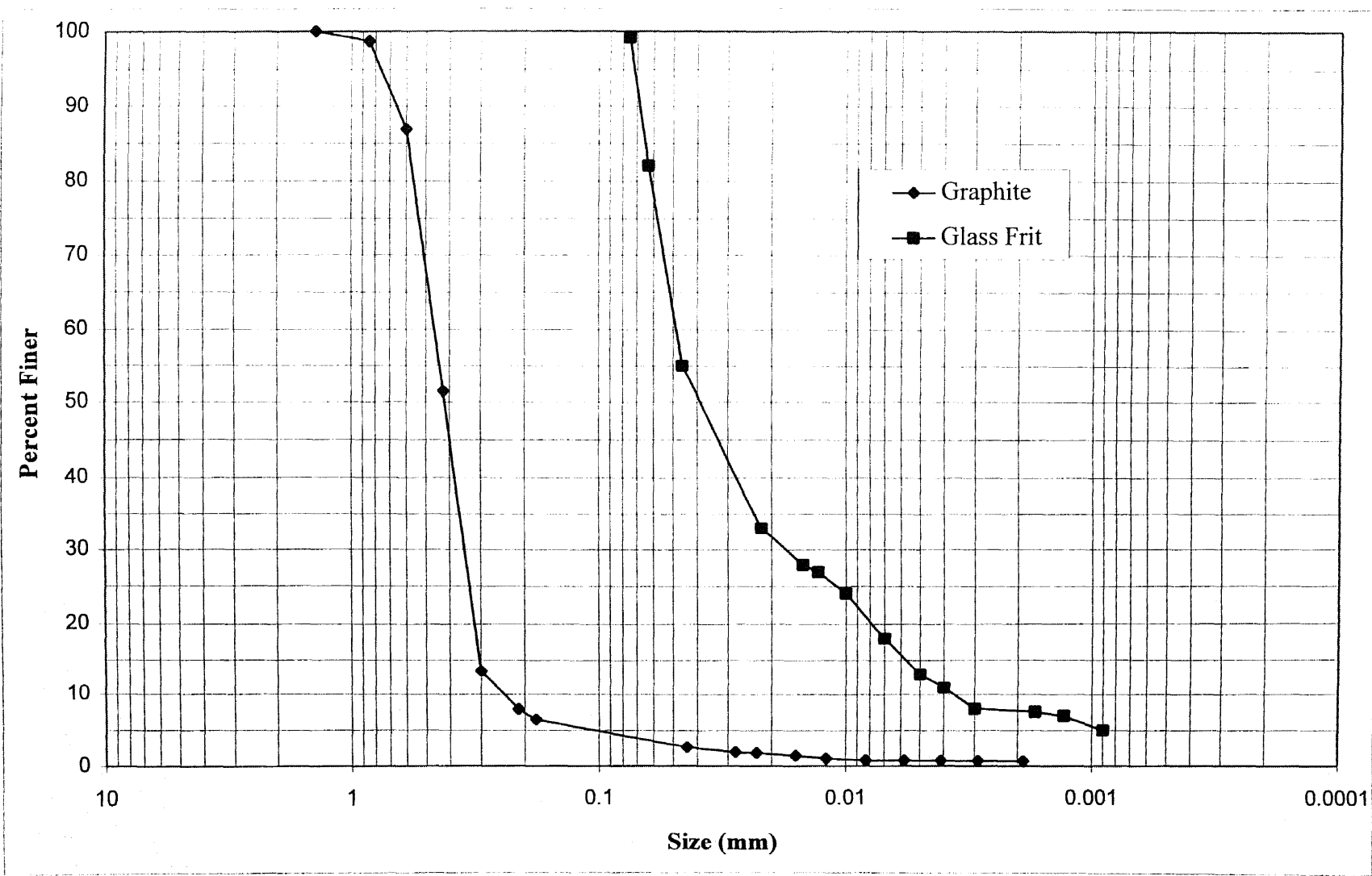
hydrometer test (ASTM, 1994).

Figure E.1 Grain Size Distribution of Graphite (1501) and Glass Frit

122

SUPERIOR GRAPHITE CO.

CHICAGO PLANT • 6540 SOUTH LARAMIE AVE., CHICAGO, ILL. 60638
708-458-0006   FAX #: 708-594-1474

Product Data Sheet

Type: NATURAL CRYSTALLINE FLAKE

Grade: 1501

Marketing Specifications

SIZE : 80 % minimum + 50 mesh

LOI % : 80 % minimum

MOISTURE % : 1.0 % maximum

VOLATILE % : 4.0 % maximum

Typical Characteristics

DISTRIBUTION :

MESH	% ON
14	0.0
20	1.3
30	11.8
40	35.4
50	38.1
70	5.5
80	1.4
-80	6.5

LOI % : 88.0 %

MOISTURE % : 0.1 %

VOLATILE % : 1.6 %

Date: 07/94
By: DJD

Information provided on this Product Data Sheet is supplied to indicate the approximate physical and chemical properties of the material. Customers are urged to independently test the material prior to application/purchase.

REFERENCES

ASTM (American Society for Testing and Materials). 1994. *Annual Book of ASTM Standards*. Volume 4.08, Soil and Rock, Philadelphia, PA.

Boggs, S. Jr. 1987. *Principles of Sedimentology and Stratigraphy*. Merrill Publishing Company, Columbus, OH.

Bjornstad, B.N. and M.T. Murphy. 1994. "Draft Report on Task 1: 300 W Test Site Evaluation." Geology and Geophysics Group. Earth and Environmental Sciences Center. Pacific Northwest Laboratory, Richland, WA.

Chien, S.F. 1993. "Settling Velocity of Irregularly Shaped Particles." Society of Petroleum Engineers of AIME (paper), SPE, February, 2-38.

Dragun, J. 1991. "Geochemistry and Soil Chemistry Reactions Occurring During Soil in In Situ Vitrification." *Journal of Hazardous Materials*, 26: 343-364.

Ganguly, U.P. 1990. "On the Prediction of Terminal Settling Velocity of Solids in Liqiud-Solid Systems." *International Journal of Mineral Processing*, 29(3-4): 235-247.

HSMRC (Hazardous Substance Management Research Center), Accutech Remedial Systems, Inc., Battelle Memorial Institute, and Battelle Pacific Northwest Laboratories. 1994. "Pneumatic Fracturing Demonstration, Tinker Air Force Base, Oklahoma City, Oklahoma." U.S. Department of Energy Office of Research, U.S. Air Force, and U.S. Environmental Protection Agency Northeast Hazardous Waste Research Center, October, 1994.

Kehle, R.O. 1964. "Determination of Tectonic Stresses Through Analysis of Hydraulic Well Fracturing." *Journal of Geophysical Research*, January 69: 259.

King, T.C. 1993. "Mechanism of Pneumatic Fracturing." M.S. Thesis, Department of Civil and Environmental Engineering, New Jersey Institute of Technology, Newark, NJ.

McDowell-Boyer, L.M., Hunt J.R., and N. Sitar. 1986. "Particle Transport Through Porous Media." *Water Resources Research*, 22(13): 1901-1921.

Nautiyal, D. 1994. "Fluid Flow Modeling for Pneumatically Fractured Formations." M.S. Thesis, Department of Civil and Environmental Engineering, New Jersey Institute of Technology, Newark, NJ.

REFERENCES
(Continued)

New Jersey Department of Environmental Protection. 1994. "List of Known Contaminated Sites in New Jersey." New Jersey Department of Environmental Protection, Trenton, NJ.

Papanicolaou, P. 1989. "Laboratory Model Studies of Pneumatic Fracturing of Soils to Remove Volatile Organic Compounds." M.S. Thesis, Department of Civil and Environmental Engineering, New Jersey Institute of Technology, Newark, NJ.

Personal Communication. 1995. Superfund Hotline, operated by Booze, Allen and Hamilton under U.S. EPA contract. (800) 424-9346. March, 1995.

Pettijohn, F.J., Potter, P.E. and R. Siever. 1973. *Sand and Sandstone*. Springer-Verlag, New York, NY.

Sakthivadivel, R. 1969. Clogging of a Granular Porous Medium by Sediment. *Rep. HEL*, Hydraulic Engineering Laboratory, University of California, Berkeley, CA., pp 15-17, 106.

Shah, N.P. 1991. "Study of Pneumatic Fracturing to Enhance Vapor Extraction of Vadose Zone." M.S. Thesis, Department of Civil and Environmental Engineering, New Jersey Institute of Technology, Newark, NJ.

Schuring, J.R. and P.C. Chan. 1993. "Pneumatic Fracturing of Low Permeability Formations." Technology Status Paper, Department of Civil and Environmental Engineering, New Jersey Institute of Technology, Newark, NJ.

Timmons, D.M., Fitzpatrick, V., and S. Liikala. 1990. "Vitrification Tested on Hazardous Wastes." *Pollution Engineering*, June, pp. 76-81.

Tsoar, H. and K. Pye. 1987. "Dust Transport and the Question of Desert Loess Formation." *Sedimentology*, 34: 139-153.

U.S. Environmental Protection Agency. 1993. "Accutech Pneumatic Fracturing Extraction and Hot Gas Injection, Phase I, Applications Analysis Report." EPA/540/AR-93/509, Superfund Innovative Technology Evaluation, Risk Reduction Engineering Laboratory, Office of Research and Development, Cincinnati, OH.

U.S. Environmental Protection Agency. 1995. "Integrating Pneumatic Fracturing and Bioremediation for the In-Situ Treatment of Contaminated Soil." Prepared by Rutgers, The State University of New Jersey and New Jersey Institute of Technology for U.S. EPA-ORD, Releases Control Branch (MS-106), Edison, NJ.